UNIVERSITY OF CALIFORNIA, SAN DIEGO

Sound reception mechanism analysis of a Cuvier's beaked whale (*Ziphius cavirostris*)

A Thesis submitted in partial satisfaction of the
requirements for the degree
Master of Science

in

Structural Engineering

by

Ivana Escobar

Committee in charge:

Professor Petr Krysl, Chair
Professor Michael Todd
Professor Joel Conte

2016

The Thesis of Ivana Escobar is approved, and it is acceptable in quality and form for publication on microfilm and electronically:

_____

_____

_____

Chair

University of California, San Diego

2016

DEDICATION

To my mentor, family, and friends. My sisters, Maria José and Christiane, and little brother Max encouraged and supported me through this process; I will forever be grateful for your compassion.

EPIGRAPH

The profound study of nature is the most fertile source of mathematical discoveries.

— Joseph Fourier

TABLE OF CONTENTS

LIST OF FIGURES

LIST OF TABLES

ACKNOWLEDGEMENTS

It goes without saying that my mentor and thesis chair, Dr. Petr Krysl, was an essential part of my progress in the last year. He allowed me to develop and learn in my own way, which is a luxury I do not take for granted. in academia, the people who care are he people who influence students the most, and I have been extremely fortunate to learn more than just technical ability from Professor Krysl. His mentorship allowed me to see a calm approach to achieving goals, which is a true quality of a professional educator and researcher.

I would like to point out that I would have spent many lonely, hungry nights if it weren't for my grandparents, Oma and Opa, who visited throughout my time in San Diego. They provided emotional support for me when I was running low, and reminded me of what I value in life and what I stand for. In my upbringing, they showed me that a life purpose should be driven by care, compassion, and unrelenting persistence.

UCSD has given me the incredible chance of meeting people from all over the world. Along with the provided education, I learned from many people about cultures I wasn't accustomed to and created bonds with colleagues and friends that will last my lifetime. I want to acknowledge Jim Pasterbar, whom provided collaborative conversation and created a safe haven of discussing technical matters without fearing the perception of stupidity.

ABSTRACT OF THE THESIS

Sound reception mechanism analysis of a Cuvier's beaked whale (*Ziphius cavirostris*)

by

Ivana Escobar

Master of Science in Structural Engineering

University of California, San Diego, 2016

Professor Petr Krysl, Chair

Anthropogenic sound in the ocean, such as sonar, has been related to mass strandings of marine life, in particular the Cuvier's beaked whale (*Ziphius cavirostris*). Since opportunities to study behavioral responses are limited, furthering our knowledge of whales through simulation has become a well adopted process [15] [5]. To simulate sound reception, the *Ziphius* ear complex was implemented as a three dimensional finite element model with two mechanisms that enable hearing; pressure loading from surrounding soft tissues and bone conduction from skull vibration. The numerical formulation was summarized to demonstrate an assumed-strain technique using nodally

integrated continuum elements (NICE) [11] for a forced harmonic vibration problem.

This work focuses on obtaining hearing responses using both mechanisms in conjunction with each other, while also looking into the effects of each mechanism individually. Mesh refinement with surface and volume smoothing reveals variations of simulated auditory response for the two loading mechanisms considered. Effects of the amplitudes and phase shifts, used in loading, along with material damping were reviewed for cases of only one mechanism applied at a time, then with both mechanisms active together.

A synthetic audiogram was generated from the stapes velocity transfer function (SVTF) based on relative displacement of the hearing structure. Results found here provide insight on the auditory sensitivity of the Cuvier's beaked whale and its ability to capture sound in the known range of mid-frequency sonar [3]. Since this marine mammal has mass strandings heavily linked to sonar activity, this work allows for an understanding of the whale's hearing over a given range of frequencies.

Chapter 1

Introduction

Background

Ziphius cavirostris are small- to medium-sized whales that span all oceanic waters deeper than 200 meters and can grow up to 7 meters in length. The Cuvier's beaked whales (*Ziphius cavirostris*) are part of the second largest family of living species in the order *Cetacea* and are the most widely distributed of any beaked whale species [8]. Beaked whales feed on deep water squid, fish, and some crustaceans living on the sea floor. From observations, it can be deduced that these whales can dive to depths of about 1,000 meters or more to feed with their dives lasting over 30 minutes, making them the deepest diving whale known to date [2].

In the process of diving, these whales will accumulate an increasing amount of nitrogen in their blood, which requires the *Ziphius* to undergo a process of decompression. To do so, the whale performs a series of interval dives, where they surface to take in new air and descend to a depth where the water pressure is enough to safely expel the presence of nitrogen [16]. If the *Ziphius* is interrupted during this process,

it runs the risk of experiencing nitrogen narcosis or even formation of bubbles in the bloodstream, also known as bends, where the worst of symptoms leads to death [3].

With an increasing amount of anthropogenic sound in the ocean, there is a necessary amount of understanding in marine life and our effect on them [9]. In the past, a high number of *Cetaceans*, beaked whales in particular, were found stranded in association with exposure to high intensity sound, such as mid-frequency sonar [3]. *Ziphius* are the species that were found stranded in higher numbers than any other species in incidents involving high-intensity sound [7]. According to the International Union for Conservation of Nature, the *Ziphius cavirostris* is currently classified as data deficient, so opportunity to further our understanding of these whales through simulation has become a well adopted process [15] [5].

Introduction

A finite element implementation of the *Ziphius* ear complex was studied to develop an understanding of the hearing ability in a range of frequencies. The model comes from a Cuvier's beaked whale anatomy found stranded at Gearhart Beach, Oregon on March 13, 2002. It was 5.15 m long and weighed 1,996 kg [7]. High-fidelity anatomic images and geometric descriptions of the structures associated with the biosonar apparatus in Cuvier's beaked whales were acquired and used in creating the mesh.

The hearing apparatus in the *Ziphius* is located along the posterior section of the mandibles (Figure 1.1). The primary component of the hearing apparatus is the organ of transduction, the dense bony ear (tympanoperiotic) complexes, referred to as TPC, which contain the middle and inner ear. Displacement of the piston-like

bone, the stapes, generates waves in the cochlear fluid which results in neural signals received by the brain.

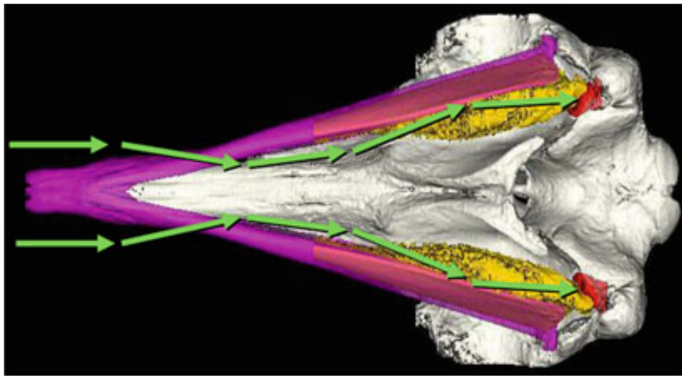

Figure 1.1: Skull view from bottom without the mandible from a scanned imaging of a Cuvier's beaked whale. The hearing apparatus, colored red, is located in the posterior structure and is connected to the skull through the periotic bone. Source: 2012 © Springer Science+Business Media, LLC [4].

Here we model the sound reception apparatus with forced harmonic vibration analysis applied to the TPC, by approximating the structure as a vibrating solid with a finite element method similar to [5] and [15]. In a previous work using the VibroAcoustic Toolkit (VATk) with voxel-based modeling techniques [9], a planar harmonic wave ensonified the entire whale skull from directly ahead. Once steady state was reached, the harmonic elastic waves acting on the whale head caused motion of the TPC through two potential mechanisms. One mechanism considered a pressure load from the mandibular fat body branches connected along the tympanic bone in the TPC. The second mechanism followed from the vibration of the skull, leading to shaking of the TPC, described as skull bone conduction as in [5]. Amplitudes and phase shifts for both mechanisms were extracted and used to load models analyzed in this work, where the driving mechanisms were later isolated for observation of their unique effects.

Loading procedures resulted in motion along the stapes footplate from which a transfer function was developed by capturing relative velocity at the footplate center for a frequency range of 10 Hz to 100 kHz. Parameters were varied to investigate their effect on the Cuvier's beaked whale hearing sensitivity, including mesh refinement, phase shifting and amplitudes involved with loading the problem, and parameters associated to viscous damping of the material. With the Stapes Velocity Transfer Function (SVTF), synthetic audiograms were constructed to visualize the ability for sound reception at a given range of frequencies for the *Ziphius*.

Chapter 2

Numerical Formulation

The TPC was modeled with forced harmonic vibration analysis for a given range of frequencies where the body acted as a vibrating solid. Spatial discretization of the equation of motion using the finite element method solved for displacements.

The boundary value problem for linear elastodynamics was considered in the strong form as

$$(S)\begin{cases} \boldsymbol{\mathcal{B}}^T\boldsymbol{\sigma} + \overline{\boldsymbol{b}} = \rho\ddot{\boldsymbol{u}} & \text{on } \Omega, \\ \boldsymbol{t}_i = \overline{\boldsymbol{t}}_i & \text{on } \partial\Omega_{\boldsymbol{t},i}, \\ \boldsymbol{u}_i = \overline{\boldsymbol{u}}_i & \text{on } \partial\Omega_{\boldsymbol{u},i}, \end{cases} \tag{2.1}$$

with notation similar to [11]. The traction boundary condition was imposed as $\boldsymbol{t}_i = \boldsymbol{\mathcal{P}}_{\boldsymbol{n}}\boldsymbol{\sigma}$. The displacement boundary condition expressed fixed displacement along its prescribed surface as $\boldsymbol{u}_i = 0$. The stress divergence, $\boldsymbol{\mathcal{B}}$, and 'vector-stress vector dot product', $\boldsymbol{\mathcal{P}}_{\boldsymbol{n}}$, operators are elaborated in Appendix A.1.

Taking Equation 2.1 as a weighted residual produces the weak form of the

problem,

$$r = \int_{\Omega} \boldsymbol{w}^T(\boldsymbol{\mathcal{B}}^T\boldsymbol{\sigma} + \overline{\boldsymbol{b}} - \rho\ddot{\boldsymbol{u}})dV - \int_{\partial\Omega_{\boldsymbol{t},i}} (\boldsymbol{t}_i - \overline{\boldsymbol{t}}_i)\boldsymbol{w}_i dA = 0 \tag{2.2}$$

Applying integration by parts via Gauss' Divergence Theorem on the first term allows for the traction term to cancel out with part of the boundary integral, where traction was defined at a value of zero when not specified by boundary conditions. The rest of the boundary integral drops out of the weak form due to the weight function being set to zero along the boundary prescribed with fixed displacements,

$$r = \int_{\Omega} -(\boldsymbol{\mathcal{B}}\boldsymbol{w})^T\boldsymbol{\sigma} + \boldsymbol{w}^T\overline{\boldsymbol{b}} - \rho\boldsymbol{w}^T\ddot{\boldsymbol{u}})dV + \int_{\partial\Omega_{\boldsymbol{t},i}} \overline{\boldsymbol{t}}_i\boldsymbol{w}_i dA = 0. \tag{2.3}$$

The total traction can split into components for the pressure loading and for damping terms by creating two subsets, $\partial\Omega_{\boldsymbol{t},i} = \partial\Omega_{\boldsymbol{p},i} \cup \partial\Omega_{\boldsymbol{d},i}$. For pressure loading, the traction term becomes $\overline{\boldsymbol{p}} = p\boldsymbol{n}$, where p is a pressure load value.

Damping was included in two forms: one due to the presence of fluid-exposed boundaries, and the second from a system-level Rayleigh damping. The first type of damping results from a plane-wave approximation on wet boundary surfaces, and was considered as a damping term because of its dependence on velocity [9]. For damping applied as an absorbing boundary condition, the term becomes $\overline{\boldsymbol{d}} = -\rho c(\dot{\boldsymbol{u}}\cdot\boldsymbol{n})\boldsymbol{n}$, where ρc can be determined as an impedance term or as is for a given material surrounding the solid.

$$\int_{\partial\Omega_{\boldsymbol{t},i}} \overline{\boldsymbol{t}}_i\boldsymbol{w}_i dA = \int_{\partial\Omega_{\boldsymbol{p},i}} \overline{\boldsymbol{p}}_i\boldsymbol{w}_i dA + \int_{\partial\Omega_{\boldsymbol{d},i}} \overline{\boldsymbol{d}}_i(\dot{\boldsymbol{u}})\boldsymbol{w}_i dA. \tag{2.4}$$

Determination of deformation involves the constitutive law for linear elasticity,

$\boldsymbol{\sigma} = \boldsymbol{D\epsilon}$, and the assumed-strain kinematic definition established in [11], $\boldsymbol{\epsilon} = \overline{\boldsymbol{\mathcal{B}}}\boldsymbol{u}$. With the residual of the weakly enforced kinematic equation,

$$r_k = \int_\Omega (\overline{\boldsymbol{\mathcal{B}}}\boldsymbol{w})^T \boldsymbol{D}(\overline{\boldsymbol{\mathcal{B}}}\boldsymbol{u} - \boldsymbol{\mathcal{B}}\boldsymbol{u})dV = 0, \tag{2.5}$$

the residuals were combined to get

$$\int_\Omega -(\overline{\boldsymbol{\mathcal{B}}}\boldsymbol{w})^T \boldsymbol{D}\overline{\boldsymbol{\mathcal{B}}}\boldsymbol{u} + \boldsymbol{w}^T\overline{\boldsymbol{b}} - \rho\boldsymbol{w}^T\ddot{\boldsymbol{u}})dV + \int_{\partial\Omega_{\boldsymbol{p},i}} \overline{\boldsymbol{p}}_i\boldsymbol{w}_i dA + \int_{\partial\Omega_{\boldsymbol{d},i}} \overline{\boldsymbol{d}}_i(\dot{\boldsymbol{u}})\boldsymbol{w}_i dA = 0. \tag{2.6}$$

An approximate solution to the boundary valued problem based on Galerkin's method takes the displacement and weight functions as interpolations with finite element basis functions over the degrees of freedom, $\boldsymbol{u} = \sum_I N_I\boldsymbol{u}_I$ and $\boldsymbol{w} = \sum_J N_J w_J$.

$$\sum_I \sum_J w_J^T [\int_\Omega (\overline{\boldsymbol{\mathcal{B}}}^T N_J^T)\boldsymbol{D}\overline{\boldsymbol{\mathcal{B}}}N_I\boldsymbol{u}_I + N_J^T\overline{\boldsymbol{b}} - \rho N_J^T N_I\ddot{\boldsymbol{u}}_I dV + \int_{\partial\Omega_{\boldsymbol{p},i}} N_{J,i}^T\overline{\boldsymbol{p}}_i dA + \int_{\partial\Omega_{\boldsymbol{d},i}} N_{J,i}^T\overline{\boldsymbol{d}}_i(N_{I,i}\dot{\boldsymbol{u}}_I)dA] = 0. \tag{2.7}$$

The strain-displacement matrix is defined as $\overline{\boldsymbol{B}}_J = \overline{\boldsymbol{\mathcal{B}}}N_J$. The equality must hold for any arbitrary test function coefficient, w_J, so the bracketed function must equal zero,

$$\sum_I \int_\Omega -\overline{\boldsymbol{B}}_J^T\boldsymbol{D}\overline{\boldsymbol{B}}_I\boldsymbol{u}_I + N_J^T\overline{\boldsymbol{b}} - \rho N_J^T N_I\ddot{\boldsymbol{u}}_I dV + \int_{\partial\Omega_{\boldsymbol{p},i}} N_{J,i}^T\overline{\boldsymbol{p}}_i dA + \int_{\partial\Omega_{\boldsymbol{d},i}} N_{J,i}^T\overline{\boldsymbol{d}}_i(N_{I,i}\dot{\boldsymbol{u}}_I)dA = 0. \tag{2.8}$$

The equation is rearranged for future convenience,

$$\sum_I \int_\Omega \rho N_J^T N_I \ddot{\boldsymbol{u}}_I dV - \int_{\partial\Omega_{\boldsymbol{d},i}} N_{J,i}^T \overline{\boldsymbol{d}}_i (N_{I,i}\dot{\boldsymbol{u}}_I) dA + \int_\Omega \overline{\boldsymbol{B}}_J^T \boldsymbol{D} \overline{\boldsymbol{B}}_I \boldsymbol{u}_I dV = \sum_I \int_\Omega N_J^T \overline{\boldsymbol{b}} dV + \int_{\partial\Omega_{\boldsymbol{p},i}} N_{J,i}^T \overline{\boldsymbol{p}}_i dA. \quad (2.9)$$

From the nature of harmonic motion, loading and displacement were described as,

$$\boldsymbol{F} = \tilde{\boldsymbol{F}} e^{i\omega t} \quad \text{and} \quad \boldsymbol{u} = \tilde{\boldsymbol{u}} e^{i\omega t}, \quad (2.10)$$

where loading, $\boldsymbol{F}$, was considered as the right hand side of Equation 2.9. Since all components of the equation include a time-dependent term, it was canceled out ($\dot{\boldsymbol{u}} = i\omega\tilde{\boldsymbol{u}} e^{i\omega t}$ and $\ddot{\boldsymbol{u}} = -\omega^2 \tilde{\boldsymbol{u}} e^{i\omega t}$) with $\tilde{\boldsymbol{F}}$ and $\tilde{\boldsymbol{u}}$ accounting for amplitudes and phase shifts. Extracting the negative sign in the damping term allowed for the discretized system to be written as

$$\sum_I \int_\Omega +\omega^2 \rho N_J^T N_I \tilde{\boldsymbol{u}}_I dV - \int_{\partial\Omega_{\boldsymbol{d},i}} i\omega N_{J,i}^T \overline{\boldsymbol{d}}_i (N_{I,i}\tilde{\boldsymbol{u}}_I) dA + \int_\Omega \boldsymbol{B}_J^T \boldsymbol{D} \overline{\boldsymbol{B}}_I \tilde{\boldsymbol{u}}_I dV = \sum_I \int_\Omega N_J^T \overline{\boldsymbol{b}} dV + \int_{\partial\Omega_{\boldsymbol{p},i}} N_{J,i}^T \overline{\boldsymbol{p}}_i dA. \quad (2.11)$$

After introducing element-wise integration, the expression can be written in matrix form as,

$$-\omega^2 \boldsymbol{M}\tilde{\boldsymbol{u}} + i\omega \boldsymbol{C}\tilde{\boldsymbol{u}} + \boldsymbol{K}\tilde{\boldsymbol{u}} = \tilde{\boldsymbol{F}}. \quad (2.12)$$

The system above was solved for a given range of frequencies, with boundary conditions applied along the surface. The mass, $\boldsymbol{M}$, damping, $\boldsymbol{C}$, and stiffness, $\boldsymbol{K}$, ma-

trices were discretized in space by linear tetrahedral elements with the nodal-integration scheme established in [11] and [10]. The locking-free continuum displacement finite elements with nodal integration (NICE elements) were selected because of their ability in avoiding volumetric locking along with allowing highly distorted elements in the discretized domain.

The stiffness matrix contains gradients of the basis functions. Instead of solving with gradients of the basis functions, a weighted average of these gradients at each node was taken using the elements connected to it,

$$\nabla \overline{N}_k(x_q) = \frac{\sum\limits_e \nabla N_k(x_q)\mathcal{J}(x_q)\mathcal{W}_q}{\sum\limits_e \mathcal{J}(x_q)\mathcal{W}_q}. \tag{2.13}$$

The node-based finite element method was developed from the assumed-strain formulation, which weakly enforces the kinematic equation along with the balance equation [10]. Robustness of NICE elements comes from replacing the inverse of the Jacobian matrix found in the gradient of the basis functions, $\nabla N_k(x_q) = \nabla N_k(\xi(x_q))\boldsymbol{J}(x_q)^{-1}$, with the transpose of its cofactor matrix, known as its adjunct matrix,

$$\nabla \overline{N}_k(x_q) = \frac{\sum\limits_e \nabla N_k(\xi(x_q))\ \mathrm{adj}(\boldsymbol{J}(x_q))\mathcal{J}(x_q)\mathcal{W}_q}{\sum\limits_e \mathcal{J}(x_q)\mathcal{W}_q}. \tag{2.14}$$

Integration was approximated using various quadrature rules. The volume integrals were evaluated using a first-order simplex nodal quadrature with equally weighted integration points located at the nodes. The surface integrals were computed using first-order Gauss quadrature with three integration points on the interior of the surface element as summarized in Table 2.1.

Table 2.1: A table of quadrature points in the isoparametric domain along with the corresponding weight for approximation of the volume and surface integrals in order from top to bottom.

Node number	Point Location ($\boldsymbol{\xi}$)			Weight
Linear Tetrahedron				
1	0	0	0	1/6
2	1	0	0	1/6
3	0	1	0	1/6
4	0	0	1	1/6
Linear Triangle				
1	2/3	1/6		1/3
2	1/6	2/3		1/3
3	1/6	1/6		1/3

The left-hand side of the formulation contains time-independent mass, damping, and stiffness matrices. The stiffness matrix was constructed on the assumption that all materials in the domain are isotropic. So the material stiffness matrix is dependent on the Young's Modulus, E, and Poisson's ratio, ν,

$$\boldsymbol{D} = \begin{bmatrix} \lambda+2G & \lambda & \lambda & 0 & 0 & 0 \\ \lambda & \lambda+2G & \lambda & 0 & 0 & 0 \\ \lambda & \lambda & \lambda+2G & 0 & 0 & 0 \\ 0 & 0 & 0 & G & 0 & 0 \\ 0 & 0 & 0 & 0 & G & 0 \\ 0 & 0 & 0 & 0 & 0 & G \end{bmatrix}.$$

where $\lambda = \frac{E\nu}{(1+\nu)(1-2\nu)}$ is the Lame‘ constant and $G = \frac{E}{2(1+\nu)}$ is the shear modulus.

The damping matrix was composed as a superimposition of the absorbing boundary conditions. The Rayleigh proportional damping described material damping where the contributions were included as a linear combination onto the mass and

stiffness matrices,

$$[C] = a_m[M] + a_k[K]. \tag{2.15}$$

The Rayleigh parameters, a_m and a_s, were determined by a minimum damping ratio, $\zeta_{min} = \frac{1}{2}(a_s\omega + a_m/\omega)$, where the minimum damping was assumed to occur at a defined frequency, ω_{min}. The parameters were found as

$$a_m = \zeta_{min}\omega_{min} \qquad \text{and} \qquad a_k = \frac{\zeta_{min}}{\omega_{min}}. \tag{2.16}$$

The applied damping considered absorbing boundary conditions of the tissue surrounding the the TPC and the cochlear fluid found in the inner ear to be elaborated in the Modeling Approach (Chapter 3).

The mass matrix was assembled as a consistent mass, but since the volume integration was approximated exclusively on the element nodes, this matrix appears as with lumped mass, or with the only non zero-values being along the diagonal. With this formulation, the problem at hand was able to be solved by defining the boundary conditions and specifying the set of frequencies.

Chapter 3

Modeling Approach

High fidelity CT scans of a beached adult male Cuvier's beaked whale found in 2012 were taken of both the body and the ear complex [7]. From these scans, an unstructured mesh was built using voxel-based discretization. Through the use of the VibroAcoustic toolkit (VATk), models were created by simulating the entire skull submerged under sea water and passing a harmonic sound waves through in the direction of head to tail. Quantities extracted, used in this work, were amplitudes and phase shifts of pressures in the soft tissues attached via mandibular fat bodies along the ear bone and of vibrations from the skull onto the attachments to the ear bone once steady state was reached. The software used to develop resutls was MATLab, with an open source code, FinEALE, available through GitHub.

In this work, the tympanoperiotic complex (TPC) was investigated because it was identified as an integral part of the hearing process [4] (Figure 3.1). The TPC contains two materials, the bone and the annular stapedial ligament, where majority of the body is composed of tympanic and periotic bone and a small ligament ring around the stapes footplate connects to the surrounding bony oval window, sealing

the inner ear.

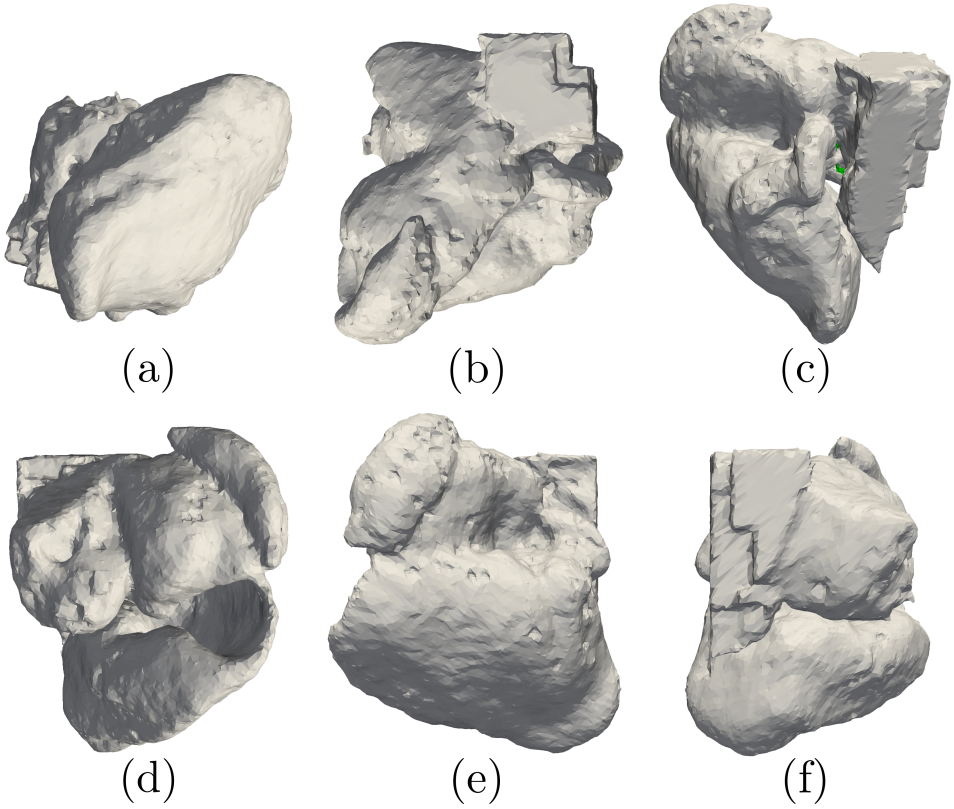

Figure 3.1: Visualization of the tympanoperiotic complex (TPC) analyzed for this study where (a) is the bottom view (b) is the top view, (c) is an isometric view, (d) is the right side view, (e) is the front view, and (f) is the back view.

Both materials were assumed as isotropic with parameters taken from previous studies [5] summarized in Table 3.1.

The footplate of the stapes has a ring of ligament material sealing the oval window (Figure 3.2), the pocket formed beneath the stapes footplate was considered to be filled with cochlear fluid.

A point was chosen on the surface of the stapes footplate, roughly in the center, and four points were selected on the periotic bone adjacent to the annular stapedial

Table 3.1: A table of materials used in all simulations performed in this study. The bone material is very stiff compared to the ligament. The stapedial ligament is not as compressible as the bone material.

Material name	Young's modulus (MPa)	Density (kg/m^3)	Poisson's ratio
Bone	30,000.0	2,470	0.30
Ligament	0.1	1,200	0.47

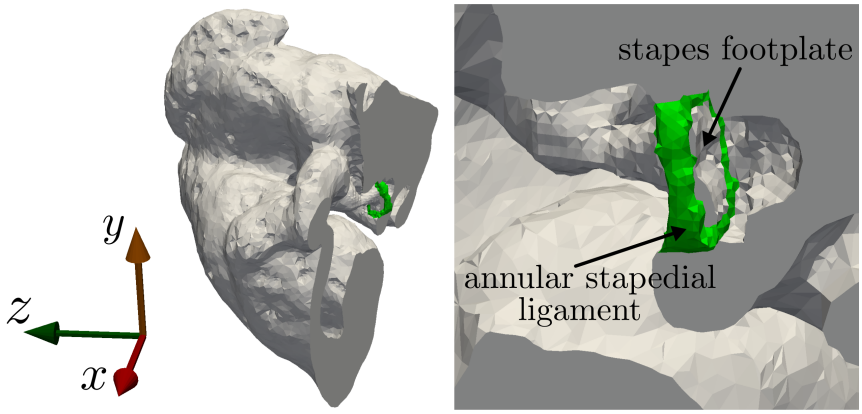

Figure 3.2: Domain clip displaying both materials. The majority of the domain consists of tympanic and periotic bone colored grey. A small ring called the annular stapedial ligament, colored green, along with the stapes footplate seal a dome filled with cochlear fluid.

ligament to extract relative displacements of the stapes footplate in the oval window. Auditory response was determined from the displacement of the stapes footplate relative to motion around the oval window (Figure 3.3).

Forced harmonic vibration analysis was run for a set of frequencies composed of sets of equally spaced intervals on a logarithmic scale that were extended to accommodate a range of frequencies from 10 Hz to 100 kHz (Appendix **??**. All conditions and applied loadings were found as linear interpolations of the extended frequencies.

The boundary conditions were imposed as contributions of bone conduction and

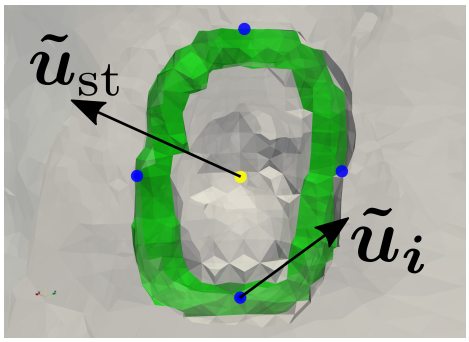

Figure 3.3: To determine the piston-like response of the stapes, four points were picked on the surrounding bone interacting with the stapedial ligament, colored blue, and the yellow point was taken as the center of the stapes footplate. The mean displacement of the four blue points was subtracted from the displacement in the center of the stapes to yield the relative movement for each frequency.

pressure loading along given surface sets. Boundary conditions and loading were all imposed as frequency dependent, where the amplitude and phase shifts were obtained from a previously generated model using VATk. This model applied sound waves hitting a *Ziphius* skull directly from the front and parameters were recorded for a given set of incident frequencies (A.2).

Since the *Ziphius* skull was assumed to be submerged in water, the incident pressure of seawater and its mechanical properties were used to normalize displacement amplitudes with

$$U_{\text{inc}} = \frac{P_{\text{inc}}}{\rho_w c_w \omega}, \tag{3.1}$$

where $\omega = 2\pi f$, P_{inc} is the incident pressure of the sound wave, ρ_w and c_w are the density and sound speed of seawater at 15°C. The list of displacement amplitudes was extended to incorporate frequencies that are both above and below the range of used incident frequencies. Phase shifts were also extended to accommodate the larger range of frequencies (Appendix A.2).

The bone conduction excitation was applied as a frequency dependent body load in all three directions with phase shifts on the second and third direction, $\bar{\boldsymbol{b}} = [\bar{\boldsymbol{b}}_x, \bar{\boldsymbol{b}}_y, \bar{\boldsymbol{b}}_z]^T$, and was imposed on all volume elements in the domain,

$$\bar{\boldsymbol{b}}_x = -\omega^2 \rho_{\text{bone}} \overline{U}_x,\ \bar{\boldsymbol{b}}_y = -\omega^2 \rho_{\text{bone}} \overline{U}_y e^{i\phi_y},\ \text{and}\ \bar{\boldsymbol{b}}_z = -\omega^2 \rho_{\text{bone}} \overline{U}_z e^{i\phi_z}. \tag{3.2}$$

The displacement amplitudes, $\overline{U}_x$, $\overline{U}_y$, and $\overline{U}_z$, and phase shifts, ϕ_y and ϕ_z, were found by interpolating values from the VATk results mentioned earlier at the incident frequencies. The density of the bone, ρ_{bone}, is found in Table 3.1.

At the bony attachment of the TPC to the entire skull, nodes were fixed to remain motionless in all three directions (Figure 3.4). This differs from previous efforts in modeling bone conduction [5], because the displacement driven mechanism was applied as a body load with fixed nodes at the connection to the skull instead of a frequency dependent essential boundary condition.

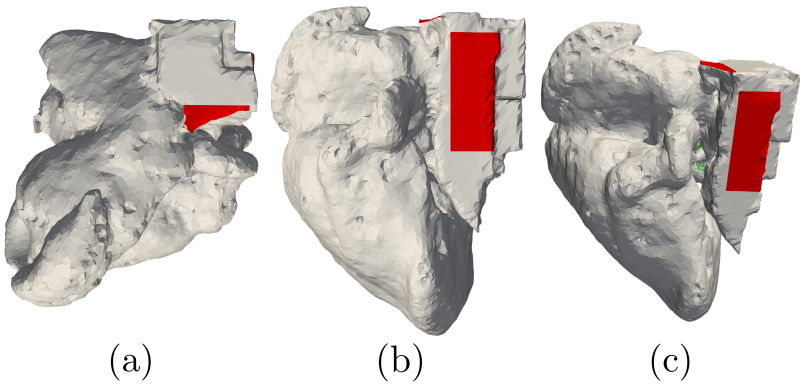

Figure 3.4: The essential boundary condition was fixed to a value of zero in all three translation directions along nodes falling within the bounding boxes colored red which are presented from the (a) top, (b) front, and (c) isometric views. For the bone conduction mechanism, this boundary condition is active in conjunction with the body load acting on all elements in the domain.

The second mechanism in this model was a pressure load applied at two patch

surfaces as traction in the normal direction. Interaction between the branches of mandibular fat bodies and TPC determined the placement of the patches [6]. Pressure amplitudes from the VATk simulations were normalized by the surrounding seawater's incident pressure, P_{inc}, and, along with its phase shifts, were extended to include frequencies above and below the range tested previously with VATk (Appendix A.2).

A frequency dependent traction loaded the TPC by pressure applied in the normal direction of the given surface with phase shifting,

$$\bar{\boldsymbol{t}} = \overline{P} e^{i\phi_p} \cdot \boldsymbol{n}, \tag{3.3}$$

where $\overline{P}$ is the pressure amplitude and ϕ_p is the phase shift, both of which are frequency dependent, and $\boldsymbol{n}$ is the outward pointing normal vector of the surface element. The pressure amplitudes and phase shifts were found in the same way as for the bone conduction mechanism, by linear interpolation of data obtained from the VATk simulations.

The pressure loading was assumed to occur on patches adjacent on the dorsal region of the domain where the tympanic bone is assumed to be connected to mandibular fat bodies (Figure 3.5). The surface elements chosen required an outward pointing normal similar to that of the surface in the center of each respective patch and a flooded connection from the center surface out to a bounding sphere.

Damping was considered due to the material itself, cochlear fluid interacting along the stapes footplate, and soft tissues in contact with the tympanic bone. Rayleigh proportional damping was assumed to have a minimum damping at 25 kHz of $\zeta_{min} = 0.025$, which made the parameters from Equation 2.16 have values of $a_m = 3.927 \,\text{E}\, 3 \ \frac{1}{s}$ and $a_s = 1.592 \,\text{E} - 7 \ s$. So, the mass and stiffness matrices were proportioned with

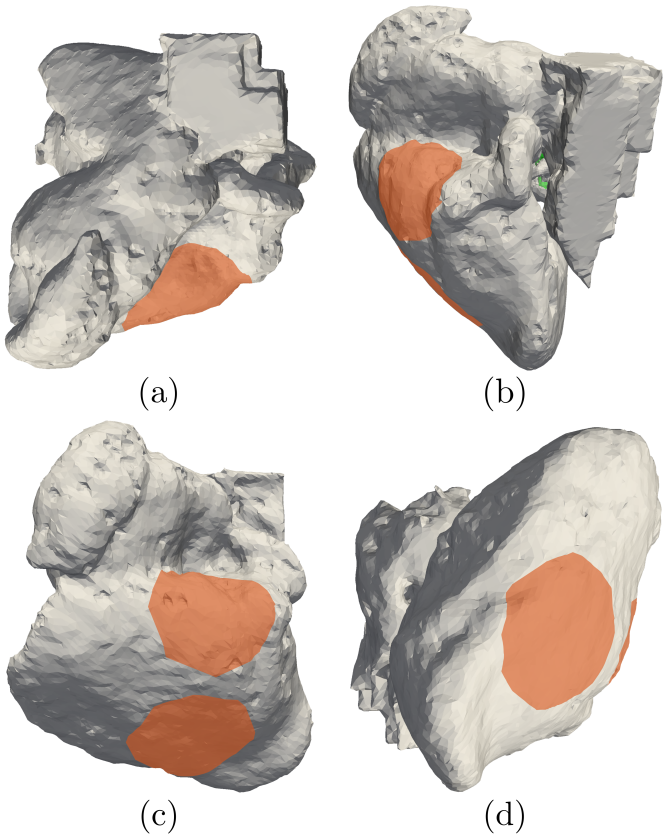

Figure 3.5: The traction boundary condition was applied on two patches whose surface elements lied entirely in the orange spots shown on the TPC, and which had an outward pointing normal similar to that of the centermost surface element. The orange patches were applied along the dorsal region of the TPC as shown from the (a) top, (b) isometric, (c) front, and (d) bottom views.

material damping using these values in Equation 2.15.

The cochlear perilymphatic fluid encased by the stapes and the dome formed by the periotic bone provided impedance as an absorbing boundary condition along the footplate of the stapes. Damping due to the cochlear fluid was applied with a resistive impedance similar to that of humans, $Z \approx 95,488$ $[\text{Pa} \cdot m^{-1} \cdot s]$ [5] [1]. This was applied on the surface of the footplate facing the dome filled by fluid, and was defined by taking the surface element closest to the center of the footplate and selecting surface elements connected to it with relatively similar outward pointing

normals.

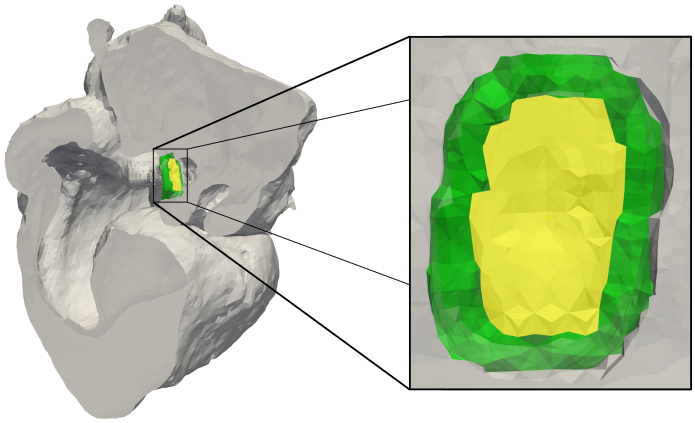

Figure 3.6: Damping due to interaction of the stapes footplate with the surrounding cochlear fluid was interpreted as a damping parameter. The surface, colored yellow, was assumed to have damping with an impedance value found from cochlear fluid of human ears due mammalian similarities among the two inner ears.

Non-coincident surface elements to those of the aforementioned pressure mechanism were selected to along the posterior section of the TPC for imposing damping from soft tissues encasing the structure (Figure 3.7). The surface was strictly selected not to overlap with the surface set determined for pressure loading so that simulations could run with both conditions applied simultaneously. The soft tissues were assumed to have mechanical properties of seawater at 15°C, and were applied with the same absorbing boundary condition technique as damping from cochlear fluid.

With these specifications, a fully loaded case was run (Appendix A.3). To further consider the effect of each individual loading type, the mechanisms were isolated into cases of bone conduction only and pressure loading only. The solutions exclusively determined from bone conduction will also be mentioned as loading by the displacement mechanism.

Relative displacement at the center of the stapes footplate was reported with

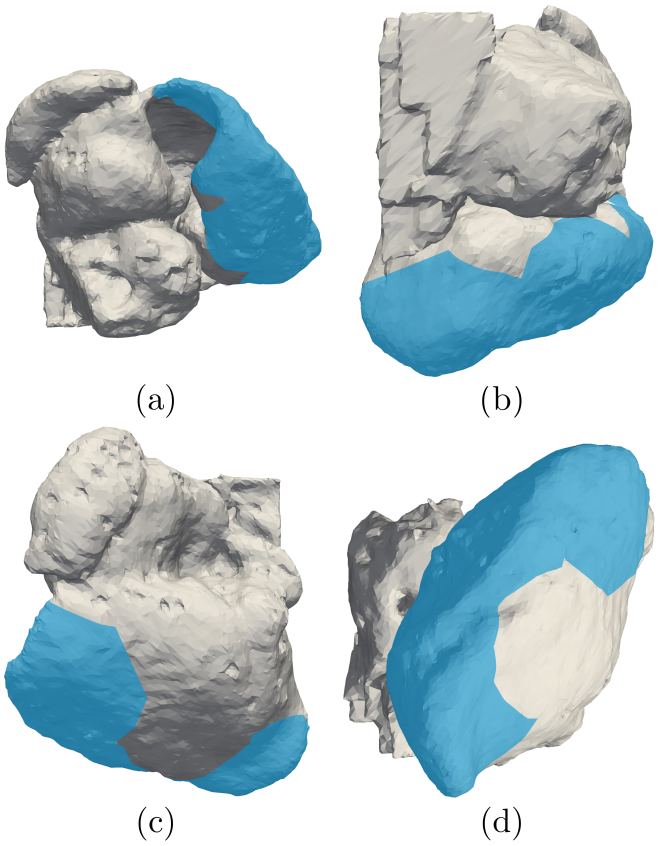

Figure 3.7: The damping boundary condition was applied on one patch whose surface elements lied entirely in the blue spots shown on the TPC. The blue patch was applied along the dorsal region of the TPC as shown from the (a) left, (b) right, (c) front, and (d) bottom views.

respect to the 'piston-like' motion of the stapes itself (Figure 3.8). Displacement at the center of the footplate, $\tilde{\boldsymbol{u}}_{\text{st}}$, was subtracted from the mean displacement of the four points chosen around the stapedial ligament, $\bar{\boldsymbol{u}}_{\text{mean}} = (\sum_{i=1}^{4} \tilde{u}_i)/4$, to obtain the relative displacement, $\boldsymbol{u}_r = \tilde{\boldsymbol{u}}_{\text{st}} - \bar{\boldsymbol{u}}_{\text{mean}}$. Finally, motion of the stapes footplate was recorded as the relative displacement that applied in the normal direction of 'piston-like' movement, $\boldsymbol{m}$, as $u_{\text{st}} = |\boldsymbol{u_r} \cdot \boldsymbol{m}|$.

The results were interpreted as the Stapes Velocity Transfer Function (SVTF), as in [5], which relates output from stapes motion to cochlear input from sound occuring underwater. From the relative motion of the stapes footplate, u_{st}, relative

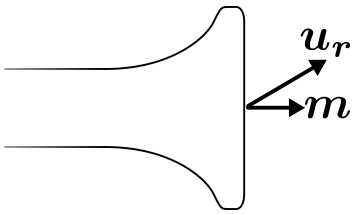

Figure 3.8: Piston-like motion of the stapes was found as back and forth movement in the direction of the normal m.

velocity at the stapes footplate was determined, $v_{\text{st}} = \omega u_{st}$, and the transfer function was found as

$$\text{SVTF} = \frac{v_{\text{st}}}{P_{inc}}. \tag{3.4}$$

Indicators for the cases where the model had only pressure loading or only displacement loading are noted as (P) and (U) respectively. In the case of full loading, simulations were run with both mechanisms active and have a transfer function indicator of (UP).

Chapter 4

Results

From the three loading cases of combined loading (UP), displacement loading (U), and pressure loading (P), Stapes Velocity Transfer Functions (SVTFs) were found using Equation 3.4. Isolated loading cases provided insight on their contribution to the most realistic loading case of both mechanisms acting in unison (UP).

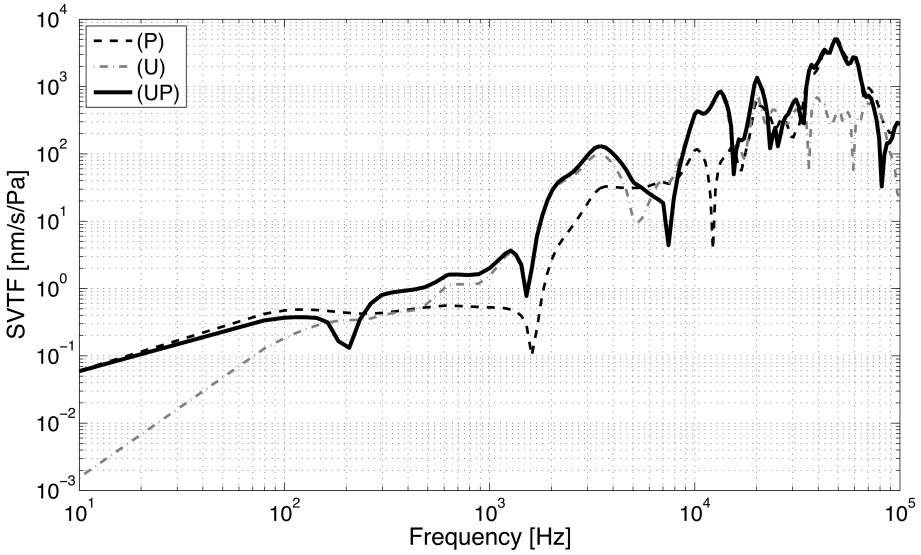

Figure 4.1: The SVTF of all three loading cases applied on the finest refinement of the mesh, Mesh 1. The solid black line represents the case of all loading mechanisms active and was considered the simulation closest to reality.

Figure 4.1 shows the hearing response was dominated by bone conduction in the mid-frequency range of about $1 - 11$ kHz. Above this range, the response had pressure loading as the leading effect between about 30 and 70 kHz.

In the interest of confirming the SVTF behavior, natural frequencies of the geometry at a coarser discretization level (Mesh 4) were used as the evaluated frequency range. The natural frequencies were found with modal analysis for all modes up to 100 kHz (Appendix A.4). It was determined that there was no need to include the natural frequencies to the range being solved for (Figure 4.2).

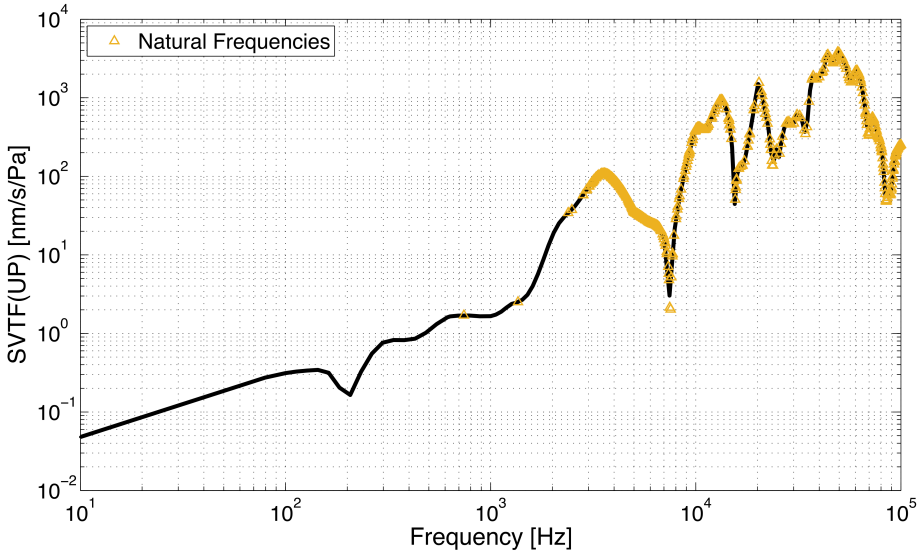

Figure 4.2: SVTF of the combined mechanisms solved at the natural frequencies (yellow triangles) and solved at the predefined range used in all simulations.

For further parametric studies, quantification of differences was measured as a relative difference compared to the base SVTF with values close to zero representing closer similarity to the original case,

$$\Delta = \frac{\|\text{SVTF} - \text{SVTF}_{\text{base}}\|}{\|\text{SVTF}_{\text{base}}\|}. \tag{4.1}$$

A measure of correlation was determined giving the least squares fit to the base SVTF. This is found by dividing each term in the SVTF by its standard deviation after subtracting the mean of the SVTF from each term,

$$\boldsymbol{s} = \frac{\mathrm{SVTF}_i - \mathrm{SVTF}_{\mathrm{mean}}}{\mathrm{SD}}, \tag{4.2}$$

where SD is the standard deviation of the given SVTF. The correlation coefficient was determined between the base, $\boldsymbol{s}_{\mathrm{base}}$, and the curve comparing to it with a value of one meaning the SVTFs being compared are completely related,

$$r = \frac{\boldsymbol{s}_{\mathrm{base}} \boldsymbol{s}^T}{\sum_{i=1} s^2_{\mathrm{base}\ i}}. \tag{4.3}$$

Both quantities determined variance from the original model with Δ describing a general change and r representing the linear relationship between curves.

Mesh Refinement Study

Using the same voxelization domain, several meshes were created beginning with the finest and coarsening with each new mesh. As the mesh was coarsened from the originally fine voxels, Laplacian smoothing on the surface and volume were applied. This led to slight changes in the domain volume for each mesh (Table 4.1). Although changes to the number of elements caused a change to the volume of the domain, the overall difference in volumes between the finest and coarsest cases remained at a 4% difference. As the number of elements increased, the volume more closely resembled the original scanned domain (Figure 3.1).

Table 4.1: A table of mesh discretization considered for this study. Since both surface and volume smoothing of the mesh were computed with each refinement the total volume of the domain is subject to differences.

Mesh No.	No. of Elements	No. of Nodes	Total Volume (mm^3)
1	527,725	96,350	39,193
2	222,975	39,544	39,062
3	130,557	23,526	38,971
4	83,917	15,444	38,829
5	57,260	10,729	38,531
6	39,700	7,610	38,135
7	27,297	5,283	37,617

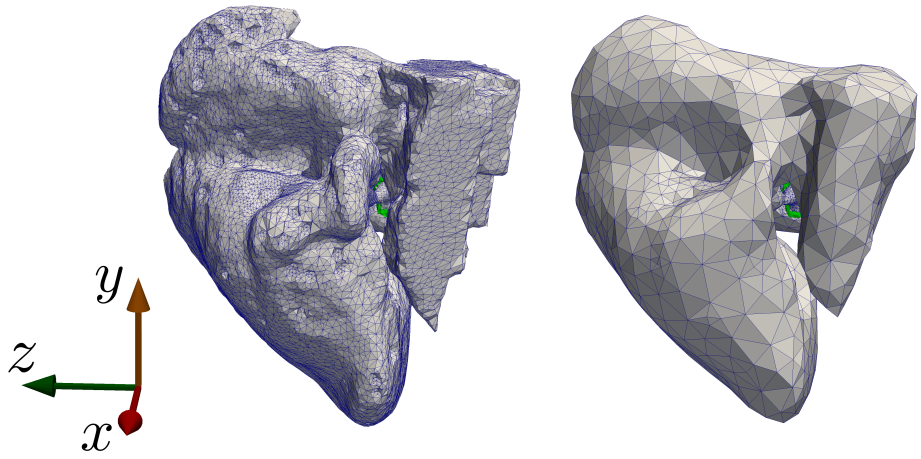

Figure 4.3: Comparison of discretization from the most refined mesh on the left to the coarsest mesh on the right. A total of seven refinements were created using both surface and volume smoothing at each interval. Note that as the mesh was coarsened the volume decreased.

The full list of discretization was applied to the most realistic case including both loading mechanisms. All seven levels of meshes were plotted along the same range of frequencies starting from the finest level and working down to the coarsest level (Figure 4.4).

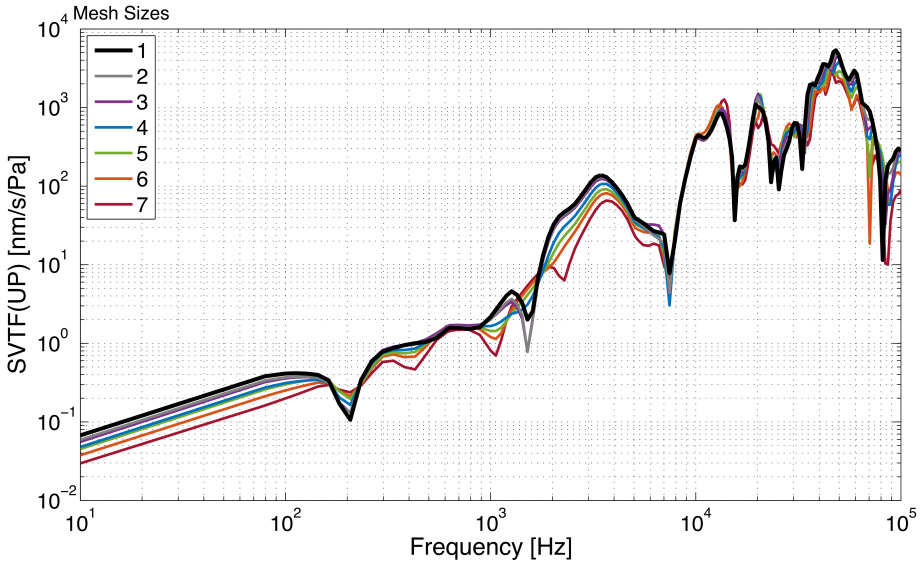

Figure 4.4: SVTF of both bone conduction and pressure loading on seven mesh discretizations, with increasing differences between curves as the mesh was further coarsened.

As the mesh was coarsened, the SVTF grew further away from the best case using Mesh 1. Comparing to the finest mesh, the largest difference was generated by Mesh 7, $\Delta = 0.497$, and the differences decreased down to a value of $\Delta = 0.113$ for Mesh 2. The lines were all above a 10% correlation, $r > 0.900$. The least correlated SVTF to Mesh 1 results was Mesh 7, $r = 0.929$, and the most correlated grew as the mesh size shrunk with Mesh 2 being correlated by $r = 0.994$. The middle mesh, Mesh 4, has a relative difference of $\Delta = 0.375$ and was correlated to the finest mesh by $r = 0.950$. With the close correlation to the original data this mesh provided similar results with a reduced amount of computation required. Detailed reporting of all the relative differences and correlation coefficients can be found in Appendix A.5.

As the mesh size grew, small features of the TPC could have been lost resulting in the nulls observed between 200 Hz and 7 kHz. All seven discretization were further investigated by isolating the individual loading mechanisms in Figures 4.5 and 4.6.

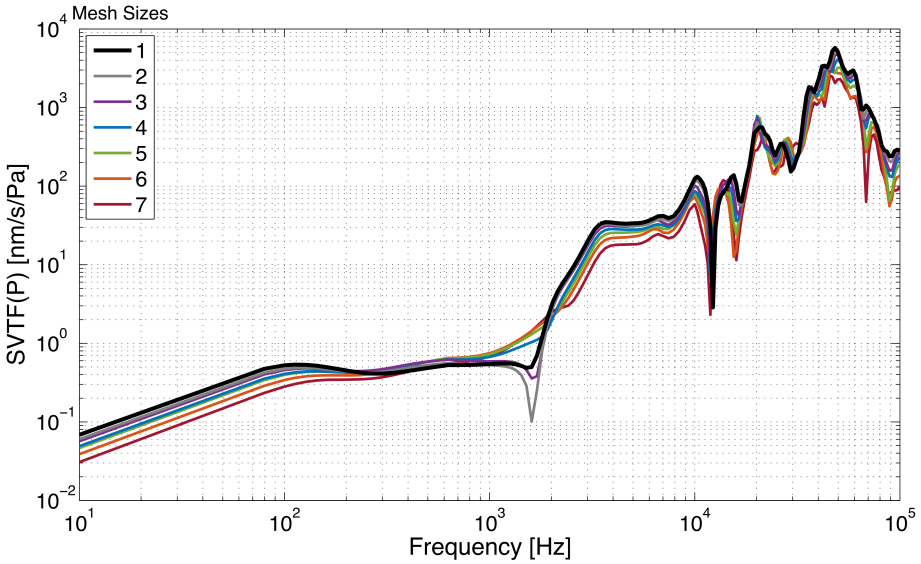

Figure 4.5: SVTF of pressure loading only on seven mesh discretization levels. Overall, the variation between the finest and coarsest mesh are qualitatively minimal, with differences potentially resulting from changes to the volume of the domain.

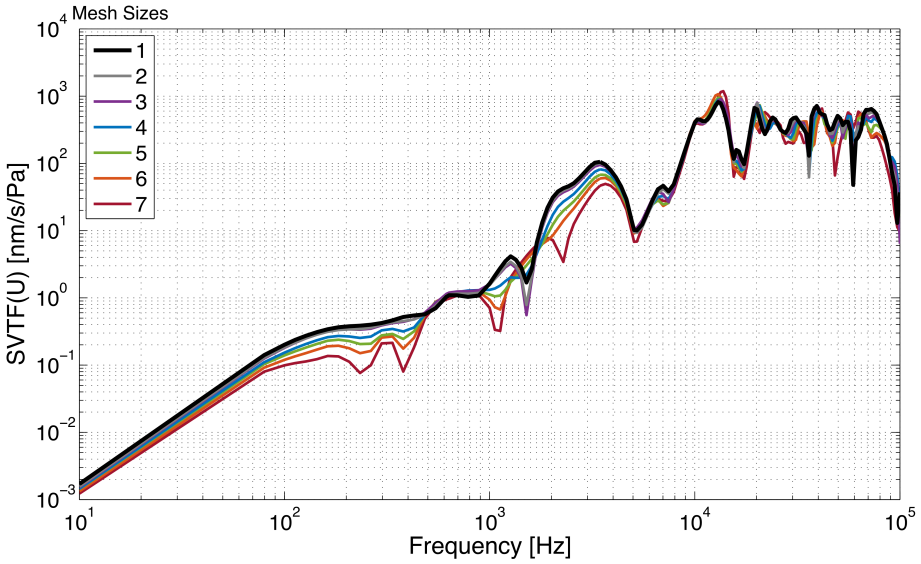

Figure 4.6: SVTF of bone conduction loading only on seven mesh discretization, with small differences between that mesh levels due to a combination of element size and volume changes.

There was no dramatic qualitative variance from the most fine results with each isolated case. In Figure 4.5, pressure loading is the isolated mechanism, and the

results are most correlated with the smallest coefficient applied on the coarsest mesh, $r = 0.966$. Mesh 7 had the most different SVTF with $\Delta = 0.533$, and Mesh 2 was the most related to the finest mesh, $\Delta = 0.111$ and $r = 0.995$. The case of only pressure loading was more correlated, and had a larger difference between meshes compared to the original SVTF using both loading mechanisms. Figure 4.6 was less correlated with the largest coefficient being $r = 0.818$. Again, Mesh 7 had the largest difference with $\Delta = 0.448$. Mesh 2 had the smallest variance from Mesh 1 with $\Delta = 0.102$ and $r = 0.990$. The case of isolating bone conduction was less correlated than the original SVTF, and had a smaller difference. The same general relationship was exhibited in the isolated cases, where as the mesh grew in size the relative difference, Δ, grew and the correlation coefficient, r, decreased indicating the SVTF was further from the most realistic solution using Mesh 1.

Further sensitivity studies were applied on the smoothed refinement of Mesh 4. This level of discretization yielded results close enough to the finest mesh, Mesh 1, while avoiding a high computation cost. Parameters under investigation were phase shifts and amplitudes for both displacement and pressure loading, minimum and damping and baseline angular frequency used for the Rayleigh proportional damping.

Phase Shift Study

The phase shift introduces an imaginary part into the problem that was investigated. The three contributing phase shifts, ϕ_x, ϕ_y, and ϕ_p, were toggled on and off. Two of which affected the bone conduction contribution, and one which affected the pressure loading (applied in Eqs. 3.2 and 3.3). Each of these phase shifts was individually toggled off, and a combination of cases was also applied (Figure 4.7).

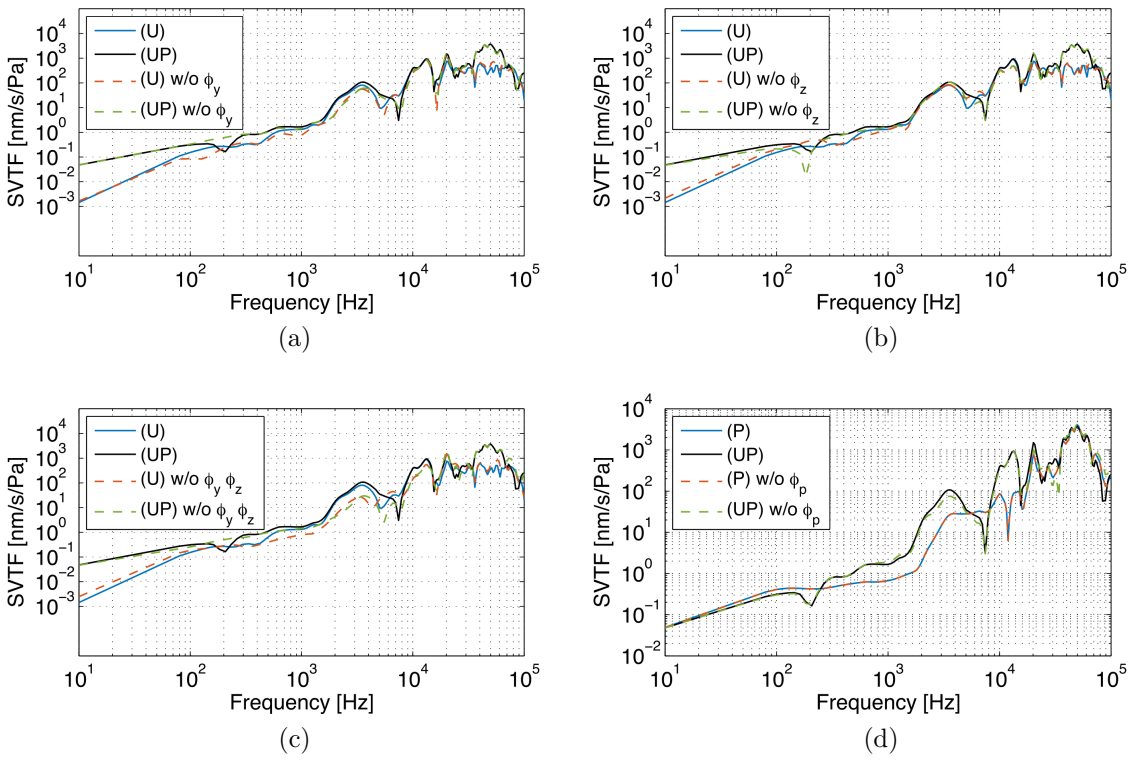

Figure 4.7: Phase shifting was toggled on and off to observe differences in the response due to changes in the type of sound received. The different cases were (a) ϕ_y off, (b) ϕ_z off, (c) ϕ_y and ϕ_z off, and (d) (a) ϕ_p off.

By turning off phase shifting individually, there was no increase to the *Ziphius*' capacity in the frequency range of 'best hearing' $(40 - 60$ kHz). In Figure 4.7, the effect of phase shifting was considered for the loading mechanism corresponding to the type of phase shift treated (U or P) along with the realistic case of all loading mechanisms active (UP). In most of the cases, removing phase shifting caused the hearing response to lose details on which frequencies cannot be heard as well as others.

Figures 4.7b and 4.7c demonstrated a peak of hearing sensitivity between $10-11$ kHz, but when the phase shifts were turned off that peak was reduced. This falsely made it seem that the *Ziphius* could not capture sound as well at those frequencies. Figures 4.7a and 4.7c showed that turning off the phase shifting caused the original

peak between 2 and 5 kHz to be smaller. This was again a misrepresentation in the hearing sensitivity of the *Ziphius*. Figure 4.7a has ϕ_y toggled off, and showed the smallest difference of $\Delta = 0.083$ with $r = 0.996$. Figures 4.7b and 4.7c had larger differences to the original SVTF of $\Delta = 0.141$ and $\Delta = 0.168$ respectively.

Toggling the phase shift corresponding to the pressure loading, Figure 4.7d, created differences in the high end of the frequency range. Between $30 - 40$ kHz, the threshold response failed to capture sensitivity with ϕ_p off and created a false null in its place. By toggling off ϕ_p, the correlation coefficient was smaller than when turning off displacement based phase shifts, $r = 0.980$. The difference between SVTFs was $\Delta = 0.194$, which was larger than the previous comparisons making the pressure related phase shift have the strongest effect on the SVTF.

By removing all phase shifts, the (UP) case displayed changed the SVTF peaks between $2 - 30$ kHz (Figure 4.8).

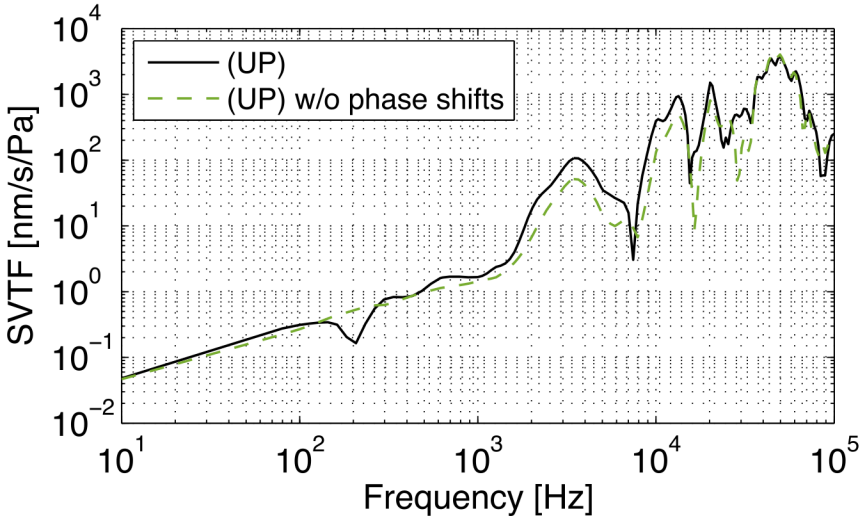

Figure 4.8: SVTF of bone conduction and pressure loading (UP) with and without all phase shifting present.

By toggling all phase shifts off, an artificial trough emerged between $30-40$ kHz

and the peaks surrounding it failed to capture the full capacity of sound reception in the TPC. A combination of errors from Figure 4.7 was displayed when not considering phase shifting at all. This case was the least correlated, $r = 0.979$, but was not the most different from the original SVTF, $\Delta = 0.194$. A fully detailed response included all corresponding phase shifting, and further results were run with ϕ_y, ϕ_z, and ϕ_p active.

Amplitude Scaling Study

Amplitudes of bone conduction and pressure loading, $\overline{U}_x$, $\overline{U}_y$, $\overline{U}_z$, and $\overline{P}$, were uniformly scaled by factors of $\frac{1}{4}$, $\frac{1}{2}$, 2, and 4. The amplitude linearly affected how much or how little body and traction loads were applied (Eqs. 3.2 and 3.3).

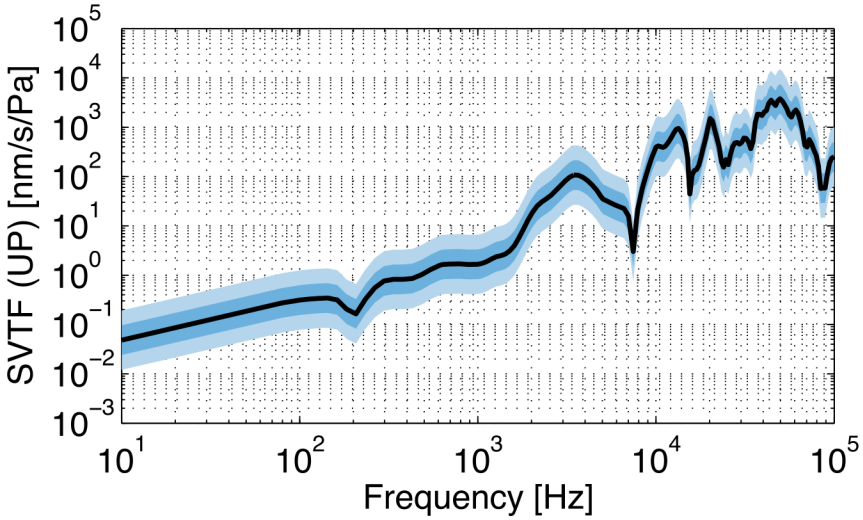

Figure 4.9: SVTF of bone conduction and pressure loading (UP), with all amplitudes scaled by factors of $\frac{1}{4}$, $\frac{1}{2}$, 2, and 4. The dark blue band corresponded to amplitudes being scaled up and down by 2. The light blue band used a scaling factor of 4 up and down.

By modifying the amplitudes, a bandwidth was created around the SVTF results for each of the cases. As the amplification grew, the curve shifted upwards,

and as the amplification was decreased, the curve shifted downwards causing the amplification correlation coefficient to be of full value in all variations, $r = 1.000$. The larger band, from 4 to 1/4 amplification, spanned over one decade giving a measure of uncertainty to the transfer function. There were no changes to the behavior of the SVTF besides vertical translation, which was expected for the case of both loading mechanisms occurring together (UP).

The isolated loading cases (U) and (P) were considered to further look into their individual effects (Figure 4.10).

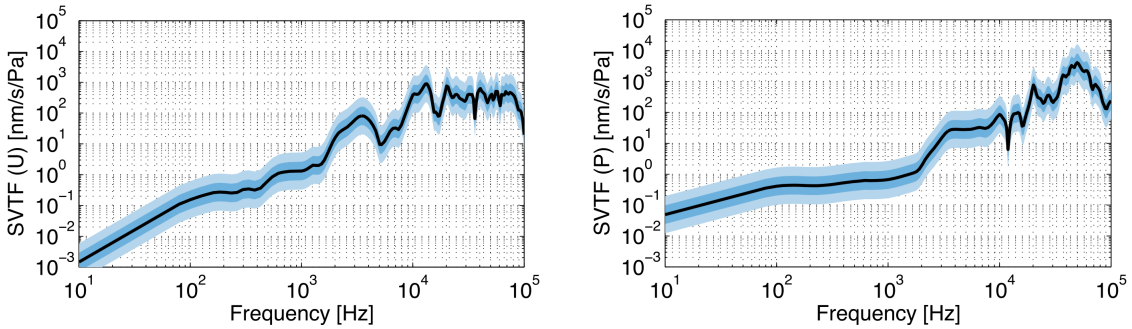

(a) (b)

Figure 4.10: SVTF with uniform scaling of the amplitudes for (a) bone conduction only and (b) pressure loading only. The dark blue band corresponded to amplitudes being scaled up by 2 and down by $\frac{1}{2}$. The light blue band used scaling factors of 4 and $\frac{1}{4}$.

Figure 4.10 showed the same effect as in Figure 4.9. As the amplification increased, the SVTF translated upwards and vice versa. This created bands around the SVTF as variations of hearing responses due to increasing or decreasing the amplifications. Since the factor was uniformly varied the SVTF was affected by a factor causing a linear variation.

Rayleigh System Damping Study

As mentioned in Chapter 2, Rayleigh proportional damping is dependent on the minimum damping ratio, ζ_{min}, and the baseline for the angular frequency, ω_{min}. Originally, the parameters had values of $\zeta_{min} = 0.025$ at a baseline frequency of 25 kHz and were increased in damping away from that frequency (Figure 4.11).

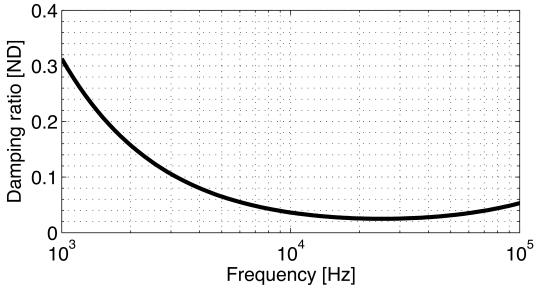

Figure 4.11: The damping ratio was dependent on frequency due to the use of Rayleigh damping. The minimum damping ratio of $\zeta_{min} = 0.025$ is found at a frequency of 25 kHz.

Both of these parameters were adjusted independently to observe differences in the SVTF by factors of $\frac{1}{4}$, $\frac{1}{2}$, 2, and 4 beginning with modifying ζ_{min} (Figure 4.12).

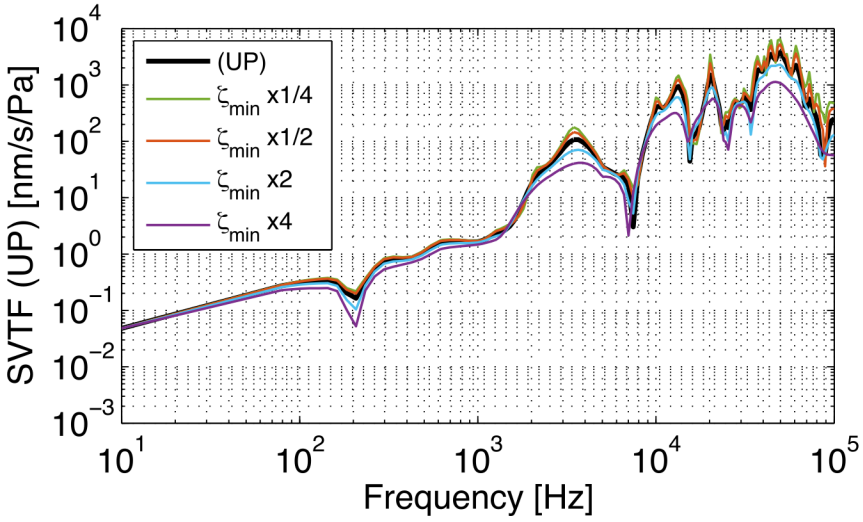

Figure 4.12: SVTF of bone conduction and pressure loading (UP), with the minimum damping ratio scaled by factors of $\frac{1}{4}$, $\frac{1}{2}$, 2, and 4.

Changing ζ_{min} from its base value of 0.025 caused modification to the intensity of peaks on the SVTF. Raising the damping ratio smoothed the curve, whereas decreasing the ratio caused peaks and troughs to grow. The lower frequencies were not as affected in the SVTF as those from $2 - 100$ kHz because the damping ration increases the further the frequency gets from its baseline of 25 kHz. The modified SVTFs were highly correlated, with the smallest correlation being $r = 0.956$. The further away from the baseline the larger relative difference was observed. The case of increasing the parameter by a factor of 4 had $\Delta = 0.648$, and the factor of 2 was smaller, $\Delta = 0.334$. Cases of isolated loading were considered next (Figure 4.13).

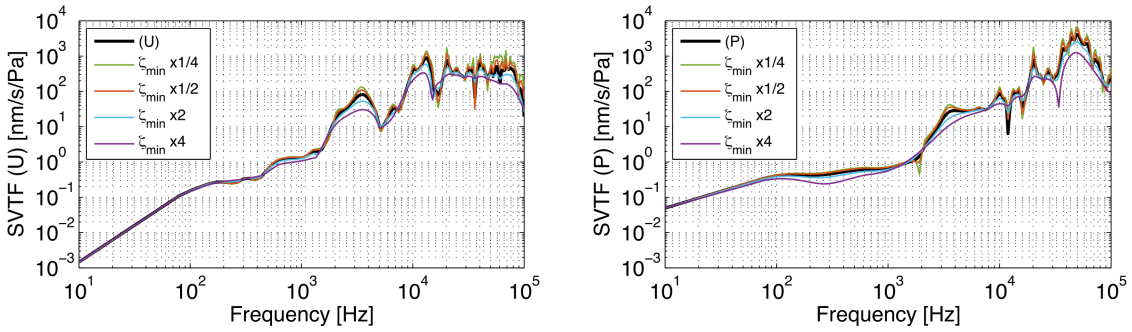

(a) (b)

Figure 4.13: SVTF with varying the minimum damping ratio, ζ_{min}, for (a) bone conduction and (b) pressure loading cases. This parameter was scaled by factors of $\frac{1}{4}$ (green), $\frac{1}{2}$ (orange), 2 (blue), and 4 (purple).

The minimum damping ratio had an effect on how the transfer function oscillated. The response had sharper peaks as this parameter decreased. Again, the lower frequencies were not affected with the exception of a bump at 300 Hz. By isolating the bone conduction mechanism, the SVTF responded more to changes of the parameter by having the lowest correlation and largest relative difference from the original case (U). Reducing ζ_{min} by 1/4 caused $\Delta = 0.707$ with $r = 0.900$, and the lowest correlation coefficient was found by increasing the parameter by a factor

of 4, $r = 0.850$. The case of pressure loading only had stronger correlation to the original SVTF (P), but the differences were larger than the case with mixed loading. The least correlated SVTF was modified by a factor of 1/4, $r = 0.972$, and the largest difference was from the case multiplied by 4 with $\Delta = 0.638$. The minimum damping ratio offered variation to smoothness of the SVTF.

The angular frequency at the minimum damping, ω_{min}, was varied from its baseline of 25 kHz by factors of $\frac{1}{4}$, $\frac{1}{2}$, 2, and 4. The frequency dependent damping ratio curve translated left with reduction of the parameter and to shift right as the baseline frequency increased (Figure 4.14).

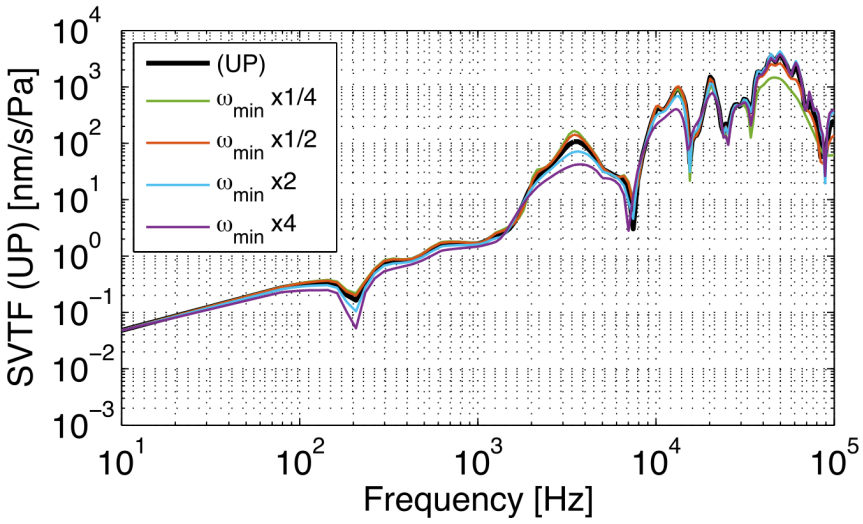

Figure 4.14: SVTF of bone conduction and pressure loading (UP), with the minimum angular frequency scaled by factors of $\frac{1}{4}$, $\frac{1}{2}$, 2, and 4.

The lower frequencies were not as affected by changing ω_{min} as the higher frequencies. At the baseline frequency, the effect of damping is minimal exhibiting the sharpest response. Damping increases the further away from the baseline the curve gets causing the SVTF to smooth out at frequencies far away from the baseline. As the parameter increased, the SVTF pivoted downwards slightly, and the opposite

behavior was found true until frequencies larger than 25 kHz. At high frequencies, the SVTF response was more sensitive as ω_{min} increased. By modifying this parameter the relative difference did not increase with larger variation from the original SVTF. As the frequency reached a lower order of magnitude, the SVTF produced varied the most from the original, $\Delta = 0.540$ and $r = 0.939$ when the angular frequency was reduced by 1/4. The closest curve was from increasing the parameter by a factor of 2 with $\Delta = 0.126$ and $r = 0.989$. The last study was run on the cases using isolated mechanisms (U) and (P) (Figure 4.15).

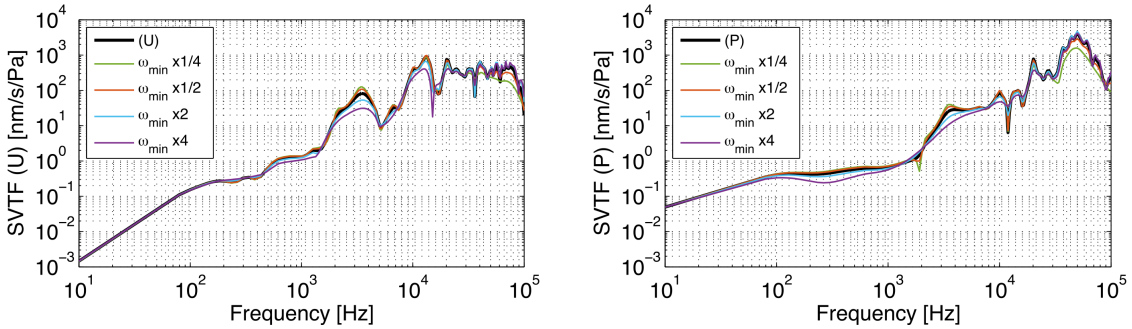

Figure 4.15: SVTF with varying the minimum frequency, ω_{min}, for (a) bone conduction and (b) pressure loading cases. This parameter was scaled by factors of $\frac{1}{4}$ (green), $\frac{1}{2}$ (orange), 2 (blue), and 4 (purple).

In the range of lower frequencies, the hearing response was reduced as the minimum angular frequency grew, once reaching about 25 kHz an opposite relationship was observed. The SVTF increased at a slightly faster rate and decreased at a faster rate after reaching the global maximum with a shrinking value of ω_{min}. This happened because of the relationship between minimum damping and the central frequency. It was observed that both isolated cases contained the largest variation in the case of reducing the baseline angular frequency by an order of magnitude (reduction by a factor of 1/4). The difference was $\Delta = 0.327$ for the case of bone conduction only (U)

and $\Delta = 0.546$ for pressure loading only (P). When isolating bone conduction, the most correlated case was the one that was increased by 2 which remained in the same order of magnitude, $r = 0.998$, but the smallest difference came by increasing the order of magnitude of the baseline angular frequency, $\Delta = 0.094$. This was different from the other cases that had the smallest difference when the parameter remained in the same order of magnitude from the original frequency.

From Chapter 2, we see that a minimum occurs at ω_{min} and changing that parameter translates the entire Rayleigh proportional damping curve to have its minimum to the left or right of its original position. This caused the part of the curve with the least amount of viscous damping to shift. The SVTF was sharper around the shifted frequency and smooth outwards from this point.

Overall, varying Rayleigh system damping parameters caused fine modifications from the original SVTF with the worst case coming from reducing the order of magnitude of the baseline angular frequency. The minimum damping ratio, ω_{min}, affected the prominence of oscillations occurring at the mid to high frequency range, and the angular frequency at the minimum condition, ω_{min}, changed the rate of ascent and descent around the central frequency.

Audiogram

To visualize hearing ability of the *Ziphius*, a synthetic audiogram was created using the SVTF with calibration to the minimal audible pressure. An audiogram is a graph used to visualize audible sound for a range of frequencies. Due to lack of behavioral data of Cuvier's beaked whales [13], the hearing sensitivities were assumed to be similar to toothed Blainville's beaked whale at 50 decibels at a reference pressure

of 1 μPa (50 dB re 1 μPa) [12] which was determined using behavioral techniques of [14]. The minimum pressure over the frequency range of $10 - 100,000$ Hz was found as

$$p_{\min} = 10^{50/20} p_{\text{ref}} = 3.162 \text{ E} - 4 \text{ Pa}. \tag{4.4}$$

The audiogram was constructed with the sound pressure levels (SPL) as the threshold pressure normalized with the reference pressure, $\text{SPL} = 20 \log p_{\text{th}}/p_{\text{ref}}$, where p_{th} is a function of the angular frequency

$$p_{\text{th}} = \frac{\max[\text{SVTF}(\omega)]}{\text{SVTF}(\omega)} p_{\min}. \tag{4.5}$$

SPL were interpreted as the intensity or volume, and the audiogram predicted audible sound for the *Ziphius* in a range of frequency from 10 Hz to 100 kHz (Figure 4.16).

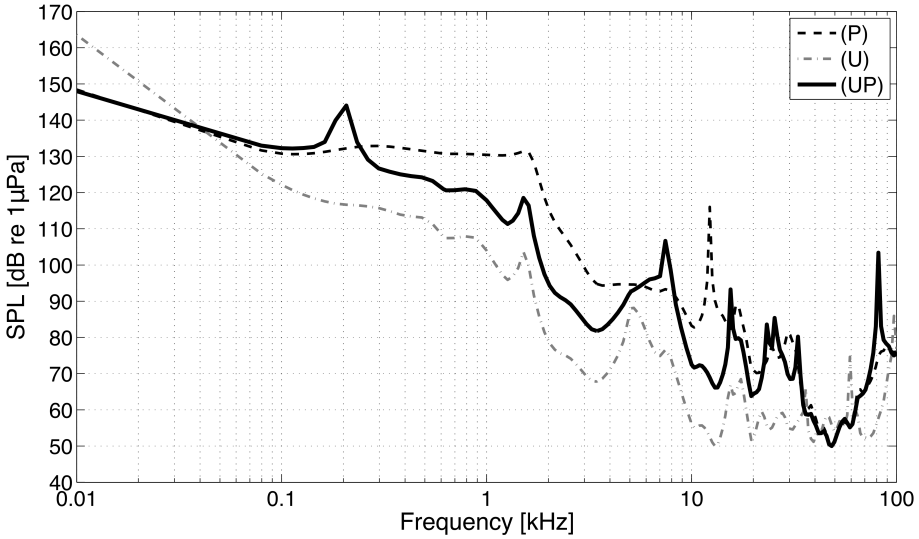

Figure 4.16: Audiogram of all three loading cases applied on Mesh 1. The lines represent an audible threshold of hearing sensitivity, where the best response occurs at 50 dB between $40 - 60$ kHz.

The point of best hearing for the *Ziphius* occurs at the minimum value of the audiogram at 48 kHz. Mid-frequency sonar has known ranges of $3 - 10$ kHz [3], and bone conduction alone (U) has a greater sensitivity when compared to the pressure loading (P) and combined cases (UP). Only looking at bone conduction for sound responses would lead to a larger range of optimal hearing from about $40 - 60$ kHz (UP and P) to $10 - 80$ kHz (U). The *Ziphius* has an estimated hearing range of 40 dB beginning from the most sensitive hearing at 50 dB, similar to previous whale simulations [5]. The range of frequencies considered audible to the Cuvier's beaked whale was from 2 to 100 kHz. This created overlap between the approximation of sound reception and the known range of mid-frequency sonar (Figure 4.17).

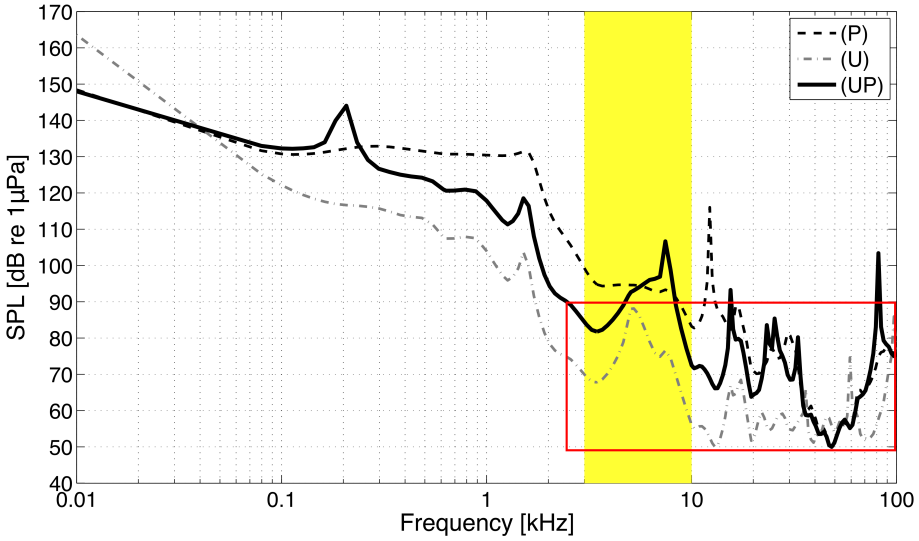

Figure 4.17: Audiogram of all three loading cases applied on Mesh 1. Known mid-frequency sonar emitted sound between $3 - 10$ kHz. The *Ziphius* has an estimated hearing range of 40 dB.

The fully loaded model involved effects of bone conduction and pressure loading acting in conjunction with each other. At the mid-frequency range it was observed that bone conduction led the response, and at higher frequencies the pressure loading mechanism led the overall hearing response. Based on this audiogram, the Cuvier's

beaked whale has the potential ability to receive sound at the levels coincident with mid-frequency sonar that are known.

Chapter 5

Conclusion

An attempt to understand sound reception of a Cuvier's beaked whale using an assumed-strain finite element method was developed from high fidelity CT scans of a beached adult male. The organ of transduction, referred to as the tympanoperiotic complex (TPC), contains the middle and inner ear. Displacement of the piston-like stapes bone lying within the TPC was modeled with a forced harmonic vibration framework for a range of frequencies from 10 Hz to 100 kHz, where the body acted as a vibrating solid.

Two driving mechanisms enabled reception of sound, bone conduction created from shaking of the TPC by the skull and pressure loading from elastic waves generated by the incident sound pressure. The most realistic case was first investigated (UP), and then each of the loading mechanisms was isolated (U and P) for further investigation of the individual contributions to the problem. 'Piston-like' motion of the stapes found relative to the oval window around the footplate was recorded to create the Stapes Velocity Transfer Function (SVTF). The SVTF was determined, and then each loading case was considered alone. From these results, a series of parametric studies

were executed using a mesh discretization that was coarser than the finest case, but exhibited close enough behavior to proceed.

Phase shifts of the driving mechanisms were varied by toggling each shift on and off individually, then together in a series of cases. The phase shifts overall did not affect the case with both mechanisms with the exception of a few locations where hearing sensitivity was falsely present. Bone conduction alone was more strongly affected, and pressure loading only was not varied when removing the phase shift.

Displacement and pressure amplitudes were scaled up and down demonstrating a band around the original SVTF with a complete correlation. This band increased upwards as the amplitude grew and decreased downwards as the amplitude shrunk. Coverage of the SVTF was determined as a range of uncertainty with the change in amplitudes of all cases.

The last parameter set studied was the minimum damping ratio and the baseline angular frequency associated with the Rayleigh proportional damping due to the material itself. By modifying the minimum damping, all cases experienced smoothing of oscillations in the SVTF as the ratio increased and sharper peaks and troughs as the ratio decreased. This parameter was the most sensitive displaying the largest relative difference when modified. The baseline frequency caused the little variation to the SVTF when maintained within the same order of magnitude. The correlation and relative difference began to grow when the baseline was reduced by an order of magnitude. When increased by an order of magnitude, ω_{min} created a stronger correlation to the original SVTF than any other variation.

Hearing ability of the *Ziphius* was visualized as an audiogram using the SVTF calibrated to the minimal audible pressure. The optimal hearing for the *Ziphius*

occurred at the minimum value of the audiogram, 48 kHz. By isolating each loading mechanism, it became apparent that bone conduction dominated sound reception in the range of $1 - 11$ kHz and pressure loading led sound reception a higher frequencies between 30 and 70 kHz. Sound reception due to bone conduction alone was the most sensitive response.

Although the *Ziphius* did not exhibit optimal hearing within the range of mid-frequency sonar, based on the estimated range of 40 dB the *Ziphius* simulated an potential to hear from $2 - 100$ kHz. Based on this audiogram, the Cuvier's beaked whale has the potential ability to receive sound at levels coincident with mid-frequency sonar that are known.

Future Work

This work was all run considering the TPC of only one side of the whale head. In humans, it is observed via behavioral responses that hearing is dominant one side over another. It would be beneficial to understand if the response in the Cuvier's beaked whale studied is different depending on what ear we are simulating responses in.

Another application of study could look into refining the mesh without modifying the volume and surface with Laplacian smoothing. Formal mesh refinement, without changing the volume, could be accomplished by beginning with the coarsest available meshed volume and refining from there. With this information, convergence studies could help determine efficiency of the specific modeling problem. Also, applying curve and volume smoothing techniques, such as Taubin smoothing, where volume shrinking doesn't occur could result in a different response for the coarser mesh.

With the intention of populating the parameter space for this problem, modifying the application of loading would allow for further insight on what sound direction is more sensitive for this mammal. This study only looked at a planar wave arriving to the skull from directly ahead, and used amplitudes and phase shifts gathered for that particular case. Varying the angle of the wave and direction could allow for a deeper understanding of the type of sound this whale is most sensitive to.

Ideally, studies such as this one could be applied to as many marine animals as data allows. Cuvier's beaked whales are historically the species most linked to strandings due to sonar activity, but there are other species that have yet to be analyzed via simulation. Since this process involves scanning a skull, these opportunities will become available indefinitely.

Appendix A

Final Notes

A.1 Finite Element Matrix Operators

The stress divergence, $\boldsymbol{\mathcal{B}}$,

$$\boldsymbol{\mathcal{B}} = \begin{bmatrix} \partial/\partial x & 0 & 0 \\ 0 & \partial/\partial y & 0 \\ 0 & 0 & \partial/\partial z \\ \partial/\partial y & \partial/\partial x & 0 \\ \partial/\partial z & 0 & \partial/\partial x \\ 0 & \partial/\partial z & \partial/\partial y \end{bmatrix}.$$

The 'vector-stress vector dot product', $\boldsymbol{\mathcal{P}_n}$,

$$\boldsymbol{\mathcal{P}_n} = \begin{bmatrix} n_x & 0 & 0 \\ 0 & n_y & 0 \\ 0 & 0 & n_z \\ n_y & n_x & 0 \\ n_z & 0 & n_x \\ 0 & n_z & n_y \end{bmatrix}.$$

A.2 VATk Model Information

The VATk model ran a wave at varying frequencies head on towards the *Ziphius cavoristis* skull to record the amplitudes and phase shifts due to displacement or pressure at given points.

The frequencies used to record amplitudes and phase shifts along the bony connections due to bone conduction were

$[78,\ 156,\ 312,\ 625,\ 1,250,\ 2,500,\ 5,000,\ 10,000,\ 20,000,\ 40,000,\ 60,000]$. This led to the following values determined by the Periotic Displacement Transfer Function (PDTF),

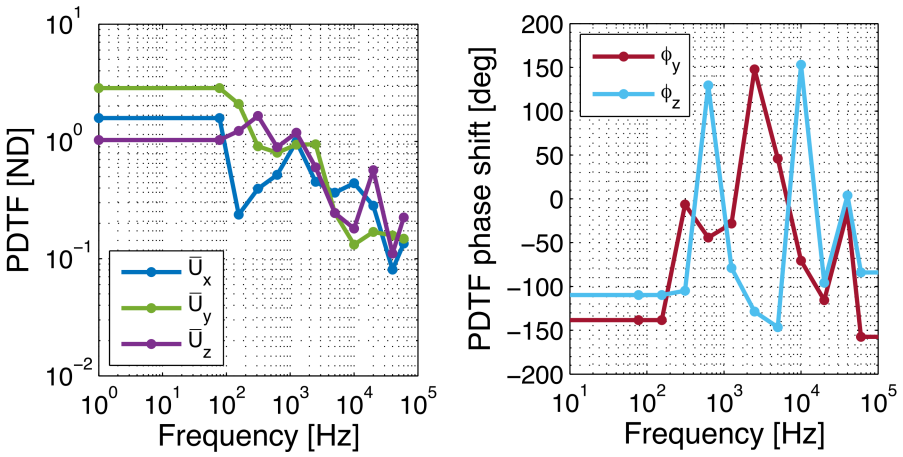

Figure A.1: The Periotic Displacement Transfer Function (PDTF) used to find the amplitudes and phase shifts determined by vibration of the ossicular chain.

The frequencies used to record amplitudes and phase shifts along the connection between the tympanic bone and the mandibular fat bodies and a pressure load were [78, 625 2,500, 5,000, 10,000, 20,000, 25,000, 30,000, 35,000, 40,000, 60,000].

This led to the following values determined by the TPC Pressure Transfer Function (TPTF),

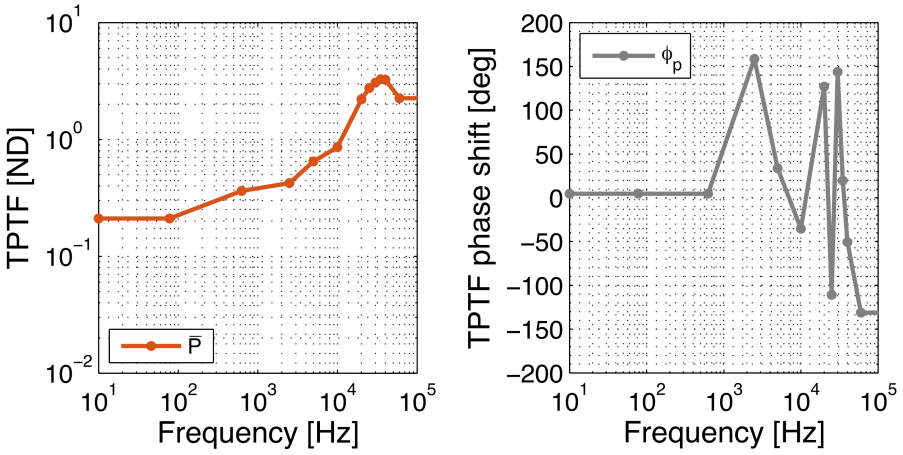

Figure A.2: The TPC Pressure Transfer Function (TPTF) used to find the amplitudes and phase shifts from sound pressure applied through the mandibular fat body branches.

A.3 Boundary Conditions

The case closest to reality uses both loading mechanisms of bone conduction and pressure loading. All conditions mentioned in Chapter 3, the domain looks to have all loadings active as shown in Figure A.3.

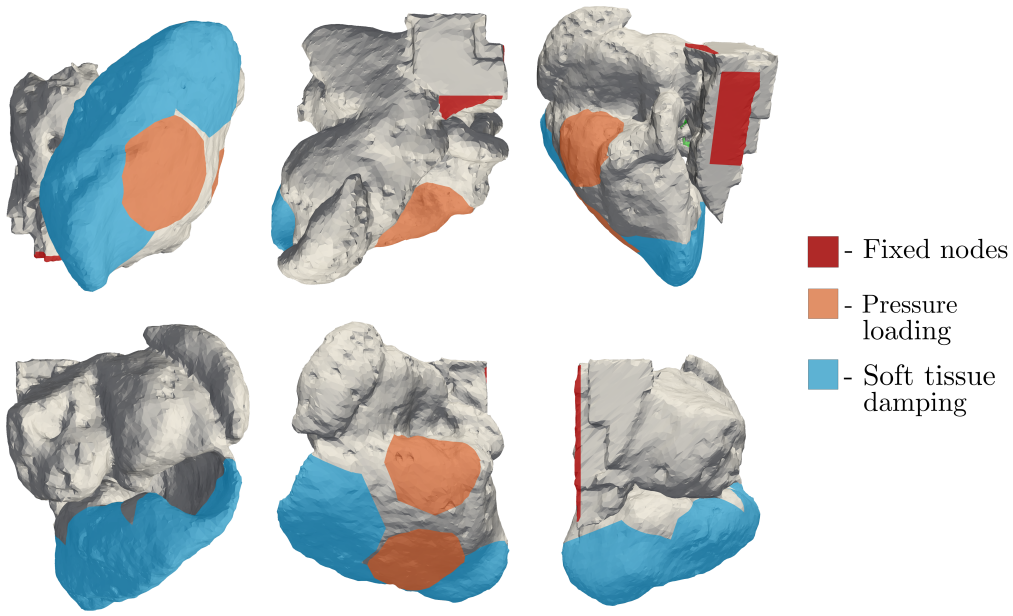

Figure A.3: Domain with all applied loading shown in multiple views. These conditions are active along with a body load, not pictured, applied on all elements.

The fixed nodes are defined as the essential boundary condition of the problem in Equation 2.1. Nodes are fixed at the connection of the periotic bone to the rest of the skull. **Bone conduction** was described as a body load applied to all elements in the volume, and was not colored in Figure A.3. Traction was applied on specified surface elements where the mandibular fat bodies connected with the tympanic bone for **pressure loading**. Soft tissue surrounding the tympanic bone dissipated energy as ramped damping, 0 Hz to 2,000 Hz and held constant after, on the prescribed surface. The stapes footplate in contact with cochlear fluid was modeled as damping

along the footplate surface.

A.4 Frequencies Used

Here is the list of frequencies used to calculate the SVTF and audiograms.

. 0.0062, 0.0229, 0.0661, 0.1419, 0.2468, 0.4171, 0.7257,
1.0e05* 0.0063, 0.0242, 0.0702, 0.1461, 0.2541, 0.4294, 0.7472,
[0.0001, 0.0070, 0.0257, 0.0744, 0.1504, 0.2617, 0.4421, 0.7693,
0.0008, 0.0078, 0.0273, 0.0790, 0.1548, 0.2694, 0.4552, 0.7920,
0.0010, 0.0089, 0.0289, 0.0838, 0.1594, 0.2774, 0.4687, 0.8154,
0.0011, 0.0100, 0.0307, 0.0889, 0.1641, 0.2856, 0.4826, 0.8396,
0.0013, 0.0106, 0.0326, 0.0943, 0.1690, 0.2940, 0.4968, 0.8644,
0.0014, 0.0113, 0.0346, 0.1000, 0.1740, 0.3027, 0.5115, 0.8900,
0.0016, 0.0119, 0.0367, 0.1030, 0.1791, 0.3117, 0.5266, 0.9163,
0.0018, 0.0127, 0.0389, 0.1060, 0.1844, 0.3209, 0.5422, 0.9434,
0.0021, 0.0134, 0.0412, 0.1091, 0.1899, 0.3304, 0.5583, 0.9713,
0.0023, 0.0143, 0.0438, 0.1124, 0.1955, 0.3401, 0.5748, 1.0000]
0.0026, 0.0151, 0.0464, 0.1157, 0.2013, 0.3502, 0.5918,
0.0030, 0.0160, 0.0492, 0.1191, 0.2072, 0.3605, 0.6093,
0.0034, 0.0170, 0.0506, 0.1226, 0.2134, 0.3712, 0.6273,
0.0038, 0.0180, 0.0522, 0.1263, 0.2197, 0.3822, 0.6458,
0.0043, 0.0191, 0.0554, 0.1300, 0.2262, 0.3935, 0.6649,
0.0048, 0.0203, 0.0588, 0.1338, 0.2329, 0.4029, 0.6846,
0.0055, 0.0215, 0.0624, 0.1378, 0.2397, 0.4051, 0.7049,

The natural frequencies of the problem were solved for using modal analysis up to a frequency of 100 kHz.

. 0.0327, 0.0381, 0.0423, 0.0463, 0.0499, 0.0536, 0.0574, 0.0629, 0.0679,
1.0e05* 0.0331, 0.0383, 0.0426, 0.0468, 0.0501, 0.0539, 0.0582, 0.0630, 0.0679,
[0.0074, 0.0332, 0.0387, 0.0426, 0.0470, 0.0501, 0.0540, 0.0589, 0.0631, 0.0689,
0.0136, 0.0337, 0.0388, 0.0429, 0.0473, 0.0504, 0.0542, 0.0590, 0.0633, 0.0689,
0.0239, 0.0344, 0.0390, 0.0434, 0.0473, 0.0506, 0.0543, 0.0591, 0.0636, 0.0696,
0.0249, 0.0346, 0.0391, 0.0436, 0.0474, 0.0508, 0.0546, 0.0592, 0.0641, 0.0701,
0.0282, 0.0348, 0.0393, 0.0436, 0.0476, 0.0509, 0.0547, 0.0595, 0.0642, 0.0701,
0.0283, 0.0351, 0.0393, 0.0437, 0.0476, 0.0511, 0.0548, 0.0597, 0.0643, 0.0707,
0.0293, 0.0355, 0.0397, 0.0441, 0.0478, 0.0512, 0.0548, 0.0598, 0.0644, 0.0709,
0.0295, 0.0358, 0.0399, 0.0441, 0.0479, 0.0513, 0.0549, 0.0601, 0.0648, 0.0713,
0.0302, 0.0358, 0.0400, 0.0443, 0.0480, 0.0517, 0.0550, 0.0602, 0.0649, 0.0722,
0.0303, 0.0360, 0.0401, 0.0443, 0.0482, 0.0518, 0.0554, 0.0603, 0.0650, 0.0724,
0.0307, 0.0361, 0.0404, 0.0446, 0.0482, 0.0520, 0.0555, 0.0607, 0.0650, 0.0724,
0.0310, 0.0362, 0.0406, 0.0446, 0.0486, 0.0522, 0.0558, 0.0608, 0.0654, 0.0734,
0.0312, 0.0366, 0.0410, 0.0450, 0.0488, 0.0523, 0.0558, 0.0612, 0.0657, 0.0738,
0.0313, 0.0369, 0.0411, 0.0450, 0.0489, 0.0523, 0.0559, 0.0613, 0.0658, 0.0740,
0.0315, 0.0371, 0.0412, 0.0452, 0.0491, 0.0525, 0.0560, 0.0617, 0.0662, 0.0747,
0.0316, 0.0372, 0.0413, 0.0453, 0.0493, 0.0527, 0.0566, 0.0618, 0.0663, 0.0755,
0.0318, 0.0374, 0.0414, 0.0455, 0.0493, 0.0528, 0.0567, 0.0619, 0.0666, 0.0761,
0.0319, 0.0376, 0.0415, 0.0458, 0.0493, 0.0530, 0.0570, 0.0620, 0.0667, 0.0769,
0.0324, 0.0379, 0.0417, 0.0461, 0.0496, 0.0532, 0.0573, 0.0624, 0.0673, 0.0770,
0.0324, 0.0379, 0.0420, 0.0462, 0.0498, 0.0534, 0.0573, 0.0624, 0.0676, 0.0771,

0.0783, 0.0990, 0.1077, 0.1354, 0.1690, 0.2311, 0.3384, 0.4756, 0.6010, 0.7191,

0.0783, 0.0991, 0.1080, 0.1355, 0.1726, 0.2323, 0.3423, 0.4766, 0.6101, 0.7239,

0.0800, 0.0992, 0.1095, 0.1358, 0.1726, 0.2346, 0.3483, 0.4821, 0.6147, 0.7267,

0.0804, 0.0994, 0.1108, 0.1367, 0.1786, 0.2358, 0.3560, 0.4917, 0.6225, 0.7292,

0.0813, 0.0995, 0.1111, 0.1408, 0.1788, 0.2382, 0.3682, 0.4976, 0.6259, 0.7294,

0.0817, 0.0999, 0.1113, 0.1446, 0.1809, 0.2420, 0.3699, 0.4999, 0.6324, 0.7351,

0.0830, 0.1005, 0.1114, 0.1448, 0.1830, 0.2479, 0.3738, 0.5099, 0.6350, 0.7375,

0.0835, 0.1007, 0.1127, 0.1455, 0.1833, 0.2565, 0.3862, 0.5129, 0.6390, 0.7441,

0.0848, 0.1019, 0.1138, 0.1455, 0.1917, 0.2605, 0.3891, 0.5156, 0.6452, 0.7508,

0.0871, 0.1025, 0.1140, 0.1465, 0.1919, 0.2640, 0.3990, 0.5202, 0.6524, 0.7518,

0.0876, 0.1030, 0.1144, 0.1467, 0.1931, 0.2756, 0.3994, 0.5211, 0.6611, 0.7576,

0.0888, 0.1033, 0.1154, 0.1467, 0.2032, 0.2758, 0.4120, 0.5304, 0.6665, 0.7616,

0.0897, 0.1042, 0.1192, 0.1476, 0.2034, 0.2771, 0.4169, 0.5371, 0.6730, 0.7700,

0.0903, 0.1043, 0.1201, 0.1477, 0.2090, 0.2817, 0.4213, 0.5427, 0.6742, 0.7729,

0.0911, 0.1045, 0.1223, 0.1493, 0.2105, 0.2863, 0.4304, 0.5533, 0.6759, 0.7753,

0.0918, 0.1046, 0.1237, 0.1557, 0.2107, 0.2866, 0.4323, 0.5587, 0.6802, 0.7795,

0.0925, 0.1046, 0.1251, 0.1567, 0.2138, 0.2909, 0.4365, 0.5627, 0.6831, 0.7825,

0.0928, 0.1049, 0.1268, 0.1569, 0.2162, 0.2923, 0.4385, 0.5709, 0.6900, 0.7885,

0.0931, 0.1053, 0.1272, 0.1579, 0.2188, 0.3003, 0.4414, 0.5715, 0.6976, 0.7974,

0.0935, 0.1053, 0.1309, 0.1581, 0.2188, 0.3007, 0.4415, 0.5716, 0.6987, 0.8013,

0.0954, 0.1054, 0.1310, 0.1618, 0.2209, 0.3087, 0.4513, 0.5782, 0.7020, 0.8024,

0.0962, 0.1059, 0.1328, 0.1621, 0.2239, 0.3119, 0.4637, 0.5830, 0.7054, 0.8060,

0.0964, 0.1064, 0.1344, 0.1647, 0.2297, 0.3210, 0.4684, 0.5920, 0.7135, 0.8077,

0.0971, 0.1066, 0.1349, 0.1677, 0.2297, 0.3255, 0.4742, 0.6000, 0.7152, 0.8141,

0.8195, 0.8439, 0.8653, 0.8863, 0.9117, 0.9309, 0.9533, 0.9742, 0.9898,

0.8224, 0.8464, 0.8676, 0.8923, 0.9179, 0.9388, 0.9586, 0.9768, 0.9917,

0.8250, 0.8501, 0.8729, 0.8985, 0.9193, 0.9415, 0.9596, 0.9802, 1.0002]

0.8316, 0.8536, 0.8756, 0.9006, 0.9256, 0.9442, 0.9637, 0.9838,

0.8349, 0.8578, 0.8813, 0.9047, 0.9289, 0.9454, 0.9644, 0.9860,

0.8385, 0.8637, 0.8838, 0.9100, 0.9301, 0.9498, 0.9675, 0.9869,

A.5 Quantitative Differences in Parametric Studies

Mesh Refinement

Table A.1: A table of relative differences, Δ, and correlation coefficients, r, when compared to the finest mesh. All refinements of the mesh were compared for a full case (UP), and by isolating the mechanisms (U and P).

	Mesh 1	Mesh 2	Mesh 3	Mesh 4	Mesh 5	Mesh 6	Mesh 7
				(UP)			
Δ	0.0000	0.1126	0.1934	0.2884	0.3752	0.4421	0.4966
r	1.0000	0.9935	0.9822	0.9653	0.9502	0.9456	0.9293
				(U)			
Δ	0.0000	0.1020	0.1688	0.2411	0.3101	0.3815	0.4479
r	1.0000	0.9897	0.9713	0.9413	0.9038	0.8591	0.8181
				(P)			
Δ	0.0000	0.1109	0.1957	0.2906	0.3845	0.4477	0.5329
r	1.0000	0.9950	0.9864	0.9731	0.9634	0.9689	0.9661

Phase Shifts

Table A.2: A table of relative differences, Δ, and correlation coefficients, r, when compared by toggling phase shifts on and off.

	ϕ_y		ϕ_z		ϕ_y, ϕ_z		ϕ_p		all ϕ
	(U)	(UP)	(U)	(UP)	(U)	(UP)	(P)	(UP)	(UP)
Δ	0.2959	0.0828	0.3102	0.1409	0.5201	0.1683	0.0000	0.1944	0.1938
r	0.9378	0.9960	0.9025	0.9868	0.8269	0.9800	1.0000	0.9796	0.9787

Amplification Factor

Table A.3: A table of relative differences, Δ, and correlation coefficients, r, when compared by varying the amplification factor by 1/4, 1/2, 2, and 4.

	1/4	1/2	2	4
	(UP)			
Δ	3.0000	0.7500	1.0000	0.5000
r	1.0000	1.0000	1.0000	1.0000
	(U)			
Δ	3.0000	0.7500	1.0000	0.5000
r	1.0000	1.0000	1.0000	1.0000
	(P)			
Δ	3.0000	0.7500	1.0000	0.5000
r	1.0000	1.0000	1.0000	1.0000

Minimum Damping Ratio

Table A.4: A table of relative differences, Δ, and correlation coefficients, r, when compared by varying the minimum damping ration, ζ_{min}, by 1/4, 1/2, 2, and 4.

	1/4	1/2	2	4
	(UP)			
Δ	0.6117	0.3254	0.3344	0.6477
r	0.9593	0.9877	0.9893	0.9558
	(U)			
Δ	0.7069	0.3286	0.2912	0.5361
r	0.9001	0.9742	0.9659	0.8492
	(P)			
Δ	0.5456	0.2991	0.3231	0.6375
r	0.9718	0.9910	0.9917	0.9728

Minimum Baseline Frequency

Table A.5: A table of relative differences, Δ, and correlation coefficients, r, when compared by varying the baseline frequency, ω_{min}, by 1/4, 1/2, 2, and 4.

	1/4	1/2	2	4
	(UP)			
Δ	3.0000	0.7500	1.0000	0.5000
r	0.9389	0.9885	0.9938	0.9829
	(U)			
Δ	0.5402	0.2451	0.1255	0.1605
r	0.9160	0.9756	0.9670	0.8763
	(P)			
Δ	0.5457	0.2438	0.1067	0.0942
r	0.9782	0.9947	0.9980	0.9944

Bibliography

[1] Ryuichi Aibara, Joseph T Welsh, Sunil Puria, and Richard L Goode. Human middle-ear sound transfer function and cochlear input impedance. *Hearing research*, 152(1):100–109, 2001.

[2] Robin W Baird, Daniel L Webster, Daniel J McSweeney, Allan D Ligon, Gregory S Schorr, and Jay Barlow. Diving behaviour of cuvier's (*Ziphius cavirostris*) and blainville's (*Mesoplodon densirostris*) beaked whales in hawai'i. *Canadian Journal of Zoology*, 84(8):1120–1128, 2006.

[3] Tara M Cox, TJ Ragen, AJ Read, E Vos, RW Baird, K Balcomb, J Barlow, J Caldwell, T Cranford, and L Crum. Understanding the impacts of anthropogenic sound on beaked whales. Technical report, DTIC Document, 2006.

[4] Ted W. Cranford and Petr Krysl. Acoustic function in the peripheral auditory system of cuvier's beaked whale (*Ziphius cavirostris*). In *The Effects of Noise on Aquatic Life*, pages 69–72. Springer, 2012.

[5] Ted W Cranford and Petr Krysl. Fin whale sound reception mechanisms: skull vibration enables low-frequency hearing. *PloS one*, 10(1):e0116222, 2015.

[6] Ted W Cranford, Petr Krysl, and Mats Amundin. A new acoustic portal into the odontocete ear and vibrational analysis of the tympanoperiotic complex. *PLoS One*, 5(8):e11927, 2010.

[7] Ted W. Cranford, Megan F. Mckenna, Melissa S. Soldevilla, Sean M. Wiggins, Jeremy A. Goldbogen, Robert E. Shadwick, Petr Krysl, Judy A. St. Leger, and John A. Hildebrand. Anatomic geometry of sound transmission and reception in cuvier's beaked whale (*Ziphius cavirostris*). *The Anatomical Record: Advances in Integrative Anatomy and Evolutionary Biology*, 291(4):353–378, 2008.

[8] Bernhard Grzimek. Mammals iv. In Michael Hutchins, editor, *Grzimek's Animal Encyclopedia*, volume 15, pages 59–66. Gale, 2 edition, 2004.

[9] P Krysl, TW Cranford, and JA Hildebrand. Lagrangian finite element treatment of transient vibration/acoustics of biosolids immersed in fluids. *International journal for numerical methods in engineering*, 74(5):754–775, 2008.

[10] P Krysl and H Kagey. Reformulation of nodally integrated continuum elements to attain insensitivity to distortion. *International Journal for Numerical Methods in Engineering*, 90(7):805–818, 2012.

[11] P Krysl and B Zhu. Locking-free continuum displacement finite elements with nodal integration. *International Journal for Numerical Methods in Engineering*, 76(7):1020–1043, 2008.

[12] Aude F. Pacini, Paul E. Nachtigall, Christopher T. Quintos, T. David Schofield, Dera A. Look, Gregg A. Levine, and Jason P. Turner. Audiogram of a stranded blainville's beaked whale (*Mesoplodon densirostris*) measured using auditory evoked potentials. *Journal of Experimental Biology*, 214(14):2409–2415, 2011.

[13] SH Ridgway and DA Carder. Assessing hearing and sound production in cetaceans not available for behavioral audiograms: Experiences with sperm, pygmy sperm, and gray whales. *Aquatic Mammals*, 27(3):267–276, 2001.

[14] Michael D Szymanski, David E Bain, Kent Kiehl, Scott Pennington, Scott Wong, and Kenneth R Henry. Killer whale (*Orcinus orca*) hearing: Auditory brainstem response and behavioral audiograms. *The Journal of the Acoustical Society of America*, 106(2):1134–1141, 1999.

[15] Andrew A Tubelli, Aleks Zosuls, Darlene R Ketten, Maya Yamato, and David C Mountain. A prediction of the minke whale (*Balaenoptera acutorostrata*) middle-ear transfer functiona). *The Journal of the Acoustical Society of America*, 132(5):3263–3272, 2012.

[16] Peter L. Tyack, Mark Johnson, Natacha Aguilar Soto, Albert Sturlese, and Peter T. Madsen. Extreme diving of beaked whales. *Journal of Experimental Biology*, 209(21):4238–4253, 2006.